

**DISTRIBUTED BRAGG REFLECTORS IN
SILICON WAVEGUIDES WITH ELEVENTH
ORDER DIFFRACTION**

A THESIS

submitted by

HARISH SASIKUMAR

for the award of the degree

of

MASTER OF SCIENCE

(by Research)



**DEPARTMENT OF ELECTRICAL ENGINEERING
INDIAN INSTITUTE OF TECHNOLOGY MADRAS.**

OCTOBER 2013

THESIS CERTIFICATE

This is to certify that the thesis titled **DISTRIBUTED BRAGG REFLECTORS IN SILICON WAVEGUIDES WITH ELEVENTH ORDER DIFFRACTION**, submitted by **Harish Sasikumar**, to the Indian Institute of Technology, Madras, for the award of the degree of **Master of Science**, is a bona fide record of the research work done by him under our supervision. The contents of this thesis, in full or in parts, have not been submitted to any other Institute or University for the award of any degree or diploma.

Dr. Deepa Venkitesh
Research Guide
Assistant Professor
Dept. of Electrical Engineering
IIT-Madras, 600 036

Dr. Bijoy Krishna Das
Research Guide
Associate Professor
Dept. of Electrical Engineering
IIT-Madras, 600 036

Place: Chennai

Date: 31st October 2013

ACKNOWLEDGEMENTS

I would like to first thank my research advisers, Dr. Deepa Venkitesh and Dr. Bi-joy Krishna Das for their guidance during this work. Their support has been a great influence to my technical and professional development during the years I spent at IITM. I wish to thank my General Test Committee members, Prof. Harishankar Ramachandran and Prof. M. P. Kothiyal for taking their time to read my reports and sit on the review meetings. Their suggestions were invaluable.

The role of Integrated Optoelectronics group in providing me with sincere feedback and their interest in my research improvements had always motivated me. I am especially thankful to Sakthivel and Sujith for the time they spent in introducing me into the fabrication and characterization processes. I wish the best to all of my other fellow labmates Shantanu, Sundar, Sidharth, Parimal, Mandar, Deepak, Rashmi, Saket, Seetha, Sireesha, Srivatsa, Chaitanya, Karthik, Dadavali, Jaseem and Vivek. I would also acknowledge my labmates who have graduated from our group -John, Gaurang, Solomon and Cebin. Their wise advices were always helpful.

I don't even have the words to express my gratitude towards my family. I would like to thank my mother and father for their dedication and for teaching me honesty, love and hardwork. My special appreciation goes to my elder brother Girish, who has always inspired me.

I would also like to thank Abhilash and Balasubramaniam of Physics department for their sincere friendship and consistent help in personal and technical matters. I am grateful to God almighty and my Guru Swami Nijananda Saraswathi whose teachings made me to remain passionate about work and life.

ABSTRACT

KEYWORDS: Silicon Photonics, Distributed Bragg Reflectors, Silicon Waveguides, Integrated Optical Filters, Higher Order Gratings, Silicon On Insulator

Grating structures are widely used for developing integrated optical devices like couplers, filters, (de-) multiplexers, interleavers, Distributed Bragg Reflector (DBR) cavities, laser sources, etc. Because of the huge prospects of CMOS compatible photonic devices in silicon-on-insulator (SOI) platform, there have been great interest to develop efficient DBR structures with single-mode silicon waveguides. In order to realize first order DBRs, a periodicity of ~ 224 nm (smallest feature size ~ 112 nm) is required to obtain a reflection peak at 1550 nm. The fabrication of such sub-micron grating structures requires stringent process control.

In this work, we have demonstrated grating structures with a feature size ~ 1.3 μm (2.4 $\mu\text{m} \leq \Lambda \leq 2.6$ μm) to be used as integrated optical DBRs with $\lambda_{\text{Bragg}} \sim 1550$ nm. The fabrication was carried out in two-step RIE process using two different masks, respectively. The first mask was used to define DBR structures (duty cycle: 50%, corrugation depth: ~ 250 nm), whereas the second mask was to define single-mode rib waveguides (rib height: 5 μm , slab height: 3.8 μm , width: 3.0 $\mu\text{m} \leq W \leq 5.5$ μm). After fabrication, the waveguide end-facets were polished to a roughness of < 200 nm before they were taken for characterizations in our end-fire waveguide coupling set-up. The characterization results of the fabricated DBRs show a reflection of $> 90\%$ and FWHM ~ 3.3 nm (estimated from transmission spectrum) for a grating length of 5.2 mm for TE polarization.

TABLE OF CONTENTS

ACKNOWLEDGEMENTS	i
ABSTRACT	ii
LIST OF TABLES	v
LIST OF FIGURES	x
ABBREVIATIONS	xi
NOTATION	xiv
1 INTRODUCTION	1
1.1 Motivation	1
1.2 Research Objective	5
1.3 Thesis Organization	5
2 BACKGROUND THEORY AND DESIGN	7
2.1 Waveguide and Guided Modes	7
2.1.1 Phase Diagram of Planar SOI Waveguide	7
2.1.2 Design of Single Mode Rib Waveguides	11
2.2 DBRs in Single Mode Rib Waveguides	15
2.2.1 Phase Diagram of DBR in Single Mode Planar Waveguide	16
2.2.2 Rib Waveguides with Higher Order DBR Structures	18
2.2.3 Choice of Diffraction Order, Periodicity and Length	21
2.2.4 Fabrication Tolerance to Design Parameters	23
2.2.5 Optimized Parameters	25
3 FABRICATION AND CHARACTERIZATIONS	26
3.1 Optical Mask Design and Fabrication	26

3.2	Process Optimization	29
3.3	List of Fabricated Devices	38
3.4	Experimental Results and Discussions	39
3.4.1	Waveguide Loss and Mode Profile	39
3.4.2	Spectral Response	44
3.4.3	Discussions	45
4	CONCLUSIONS	49
4.1	Summary	49
4.2	Outlook	50
A	DERIVATIONS	52
A.1	Calculation of Coupling Coefficient	52
B	PROGRAMMING	55
B.1	RSOFT Code Representing a Rectangular Element	55
B.2	C Code for Generating the RSOFT Elements	56
B.3	MATLAB Code for Computing the Fourier Coefficients of a Trapezoidal Structure	58
C	FABRICATION CHEMISTRY	60
C.1	Photoresist Developer	60
C.2	Chromium Etchant	60
C.3	Piranha Solution	60

LIST OF TABLES

2.1	Optimized design parameters for integrated optical DBR structure with large cross-section rib waveguide structure.	25
3.1	Specifications of the mask plate.	28
3.2	Specifications of the silicon wafer used for optimizing the fabrication processes.	29
3.3	Specifications of the SOI wafer used for fabricating the devices.	29
3.4	Parameters used for the spin coating of PPR.	30
3.5	Optimized timings for prebake, exposure, post-exposure bake and development. The temperatures used and the typical lab ambient conditions measured during the process are also given.	31
3.6	Recipe used for RIE in the realization of gratings (Recipe1).	32
3.7	Recipe used for RIE in the realization of waveguides (Recipe2).	34
3.8	List of some of the important silicon samples. These samples were used for optimizing the fabrication processes as well as for studying the surface profiles.	38
3.9	List of some of the important SOI samples. These samples were used for both optical characterizations as well as for studying the surface profiles.	39
3.10	Final parameters of the integrated optical DBR structure on large cross-section rib waveguides after fabrication.	48

LIST OF FIGURES

1.1	Schematic diagram of a distributed Bragg reflector (DBR). The periodic refractive index variation results in the reflection of the phase-matched wavelength (λ_B). Λ is the period of the DBR. Here, refractive indices n_1 and n_2 are used alternatively to represent the DBR structure.	2
1.2	Various geometries of DBRs in SOI platform: (a) Surface corrugation in rib structure, (b) Surface corrugations in rib and slab, (c) Sidewall corrugations, (d) Implantation of oxide or defect inside the volume of the waveguide.	3
1.3	Schematic representation of phase matching due to higher order diffraction in a DBR. Solid black lines in the left side indicate the spatial distribution of refractive index in one of the periods of a hypothetical rectangular-grating. Solid red lines in the left side indicate the electric field distribution of an arbitrary input signal. Dashed black lines in the right side are the spatial harmonic components of the rectangular grating and the dashed red lines in the right side are the the components of the signal which are phase matched and reflected due to the corresponding grating harmonic.	4
2.1	Phase diagram of a monochromatic wave with a wavelength λ_0 propagating in bulk silicon (with refractive index n_{Si}).	8
2.2	Phase diagram of a monochromatic wave with a wavelength λ_0 propagating in a multimode planar waveguide in SOI substrate.	9
2.3	Phase diagram of a monochromatic wave with a wavelength λ_0 propagating in a single mode straight waveguide. n_{eff} is the effective index of the guided mode in the waveguide. k_0 is the phase constant in freespace. Hence, $k_0 n_{SiO_2}$, $k_0 n_{Si}$ and $k_0 n_{eff}$ are the phase constants in the SiO_2 , Si and Si singlemode waveguide.	10
2.4	Schematic view of a large cross-section rib waveguide. Typical values for single mode waveguiding: $H = 5 \mu m$, $h \sim 3.8 \mu m$, $W \sim 5 \mu m$. Fundamental mode size is comparable to standard single mode fiber.	11

2.5	Graphical representation of choosing waveguide parameters for a SOI device layer thickness of $5 \mu\text{m}$. The dimensions satisfying single mode condition (at wavelength, $\lambda \sim 1550 \text{ nm}$.) are demarcated using the solid black line and the hatched region below it. Dimensions with larger slab heights (red) are avoided due to increased bend losses. Waveguide widths in the blue region are preferred for efficient fiber-chip coupling. The allowed dimensions are indicated in green colour.	13
2.6	Effective index of TE modes in the rib waveguide with $H = 5 \mu\text{m}$, $h = 3.8 \mu\text{m}$ for $\lambda = 1550 \text{ nm}$	14
2.7	The typical mode profiles for (a) $W=3 \mu\text{m}$ and (b) $W=6 \mu\text{m}$ for TE polarization obtained using RSOFT MODE Solutions TM . As the waveguide width increases, the mode gets more confined in the rib region.	15
2.8	Phase diagram of a monochromatic wave with a wavelength λ_0 propagating in a single mode waveguide (see Fig. 2.3) with gratings.	16
2.9	Phase diagram of a monochromatic wave with a wavelength λ_0 propagating in a single mode waveguide with DBRs. The wavelength λ_0 is phase matched with period of the DBR structure.	17
2.10	Phase diagram of a monochromatic wave with a wavelength λ' propagating in a single mode waveguide with DBRs. The wavelength λ' is not phase matched with period of the DBR structure.	18
2.11	Schematic view of DBR structures on a large cross-section rib waveguide ($H = 5 \mu\text{m}$, $h \sim 3.8 \mu\text{m}$, $W \sim 5 \mu\text{m}$)	19
2.12	The mode profile (TE polarization) of a waveguide with the typical dimensions as given in Fig. 2.11 caption. Parts of the mode profile overlapped with etched grating structure is demarcated by hatching. X_{G1} , X_{G2} , Y_{G1} and Y_{G2} are the coordinates defining the limits of integration in the evaluation of overlap integral. The regions of integration are: (1) $X_{G1} < x < \infty$, $0 < y < Y_{G1}$, (2) $X_{G2} < x < \infty$, $Y_{G1} < y < Y_{G2}$ and (3) $X_{G1} < x < \infty$, $Y_{G2} < y < \infty$	20
2.13	The variation of total overlap integral (blue) as a function of waveguide width, W . Overlap integral due to gratings in slab (black) and rib (red) regions are indicated separately.	21
2.14	(a) Reflection spectrum as a function of phase matching, $\Delta\beta$ for some typical values of κ and a grating length of 2 mm . (b) Variation of $\Delta\beta(\lambda) = 2\beta_1 - m\frac{2\pi}{\Lambda}$ as a function of λ . The zero phase mismatch and hence the reflection peak for 11 th order diffraction occurs at $\lambda_B \sim 1560 \text{ nm}$ for a grating period, $\Lambda = 2.5 \mu\text{m}$	22
2.15	The variation of peak reflectivity as a function of grating length for various waveguide widths.	22

2.16	Normalized reflectivity corresponding to various diffraction orders for (i) rectangular gratings, (ii) trapezoidal gratings with an inclination 10° and (iii) symmetric triangular gratings.	23
2.17	The variation of reflectivity for first order and 11 th order rectangular gratings as a function of duty cycle (p). The reflectivities are in turn normalized to the maximum reflectivity in the corresponding orders.	24
3.1	Mask layouts used for the fabrication of integrated optical DBR structures in SOI. Regions in the first mask (red), the second mask (violet) and both (green) are shown in different colors. The structures marked in the layout are (1) slab, (2) alignment markers and (3) polishing markers.	27
3.2	Fabrication process flow of DBR grating structure with large cross-section single-mode rib waveguides.	30
3.3	Scanning electron microscopic image of (a) slab and (b) gratings after RIE using Recipe1. The figures show the verticality of the sidewalls as well as the surface roughness introduced in the etched region.	32
3.4	Microscopic image of (a) metal mask and (b) PPR mask after development. Due to high aspect ratio of the metal strips ($\sim 1 \mu m \times 550 \mu m$) they got removed and displaced from the sample surface during development in sample 5.	33
3.5	Reconstructed image of slab region using confocal microscopy. The red plane in the top image shows the vertical observation plane and the bottom figure shows the etch profile in that plane. A small lateral misalignment between the first and second mask processes is evident from the kink in the vertical edges of profile.	34
3.6	Comparison of the etch rates of Recipe1 and Recipe2. The etch rates were calibrated by 6 runs of RIE using each of the two recipes. The etch rates were found to be constant. The etch rates of Recipe1 and Recipe2 are $\sim 0.2 \mu m/min.$ and $\sim 0.35 \mu m/min.,$ respectively.	35
3.7	A typical scanning electron microscopic image zoomed in the grating regions for precise measurement of duty cycle.	35
3.8	The confocal microscopic image showing the uniformity of the fabricated device. The figure in the inset is a reconstructed image from the depth measurements using the confocal microscope.	36

3.9	Typical microscopic images of the SOI edges after various grades of polishing. The roughness of the polishing film is gradually reduced from $30\ \mu\text{m}$ to $100\ \text{nm}$. Correspondingly, the roughness in the edges also reduces. The rib and slab edges are clearly visible after the polishing with the $100\ \text{nm}$ rough films.	37
3.10	Schematic of the setup for measuring the transmission characteristics of the fabricated devices: TLS-Tunable Laser Source, PC-Polarization Controller, FM-Fiber Mount, L_C -Collimating Lens, P-Polarizer, L_F -Focusing Lens, DUT-Device Under Test, I-Iris, OSA-Optical Spectrum Analyser.	40
3.11	Photograph of the setup for measuring the transmission characteristics of the fabricated devices: TLS-Tunable Laser Source, FM-Fiber Mount, L_C -Collimating Lens, P-Polarizer, L_F -Focusing Lens, DUT-Device Under Test, I-Iris, OSA-Optical Spectrum Analyser.	40
3.12	Normalized transmission spectrum for TE polarization through a rib waveguide ($H=5\ \mu\text{m}$, $h=3.8\ \mu\text{m}$ and $W=3.5\ \mu\text{m}$). The measured FSR of $40\ \text{pm}$ and the estimated value is $36\ \text{pm}$ for a waveguide length of $\sim 9.3\ \text{mm}$	41
3.13	Photograph of the setup for measuring the mode profile of the fabricated devices: PC-Polarization Controller, FM-Fiber Mount, L_C -Collimating Lens, P-Polarizer, L_F -Focusing Lens, DUT-Device Under Test, Cam-Camera	42
3.14	Observed mode profile for TE input polarization at $\lambda \sim 1530\ \text{nm}$ for waveguide width, $W = 3.5\ \mu\text{m}$. This well confined mode confirms the proper guiding of light through the rib structure. Comparing this profile with the mode profile obtained from a standard single-mode fiber, the size of the mode was estimated to be $\sim 8\ \mu\text{m} \times 15\ \mu\text{m}$ (tolerance in measurement $2\ \mu\text{m}$).	43
3.15	Observed grating responses from the fabricated samples for TE polarization. The parameters of the fabricated device are: $\Lambda = 2.6\ \mu\text{m}$, $e = 260\ \text{nm}$, $L = 5.2\ \text{mm}$, $H = 5\ \mu\text{m}$, $h = 3.8\ \mu\text{m}$. The width, W is varied from $5.5\ \mu\text{m}$ to $3.5\ \mu\text{m}$. The spectrum is normalized with the transmission spectrum of waveguides and for a peak output power of $1\ \text{mW}$	44
3.16	Observed mode profiles for TE and TM input polarizations for phasematched ($\lambda = 1560\ \text{nm}$) and phasemismatched ($\lambda = 1530\ \text{nm}$) wavelengths for waveguide width, $W = 3.5\ \mu\text{m}$. The reduction in the transmitted power for TE polarization for phasematched wavelength is observed in the reduced intensity of the corresponding mode.	45
3.17	Normalized transmission at phasematched wavelength as a function of polarization angle. This figure shows the polarization dependence of the device.	46

3.18	Histogram of peak reflectivity obtained from the final devices. In total 19 devices were found to be having more than 50% reflectivity.	47
4.1	Schematic of the modified design. DC: Directional Coupler, DBR: Distributed Bragg Reflectors, P_{in} : Input Port, $P_{1,2,3}$: Output Ports.	51
B.1	Representation of a typical mask element (segment 5069) in the RSOFT CAD tool. The beginning of the element is defined relative to the beginning position of the previous element (segment 5068) where as the width ($5 \times \mathit{separation}$) and the thickness ($\mathit{period}/2$) of the element are defined in terms of absolute lengths. period and $\mathit{separation}$ are variables defined at the beginning of the code .	55

ABBREVIATIONS

Acronyms

Cam.	Camera
C-Band	Conventional Wavelength Band (1527 to 1567 nm)
CCD	Charge Coupled Device
CMOS	Complementary Metal Oxide Semiconductor
DBR	Distributed Bragg Reflector
DFT	Discrete Fourier Transform
DI water	De-ionized water
DUT	Device Under Test
FFT	Fast Fourier Transform
FM	Fiber Mount
FSR	Free Spectral Range
FWHM	Full Width at Half Maxima
I	Iris
ICP	Inductively Coupled Plasma
i-line	UV radiation of 365 nm wavelength (used for photolithography)
IR	Infra Red
L-Band	Long Wavelength Band (1567 nm to 1607 nm)
L_C	Collimating Lens
L_F	Focusing Lens
MMI	Multimode Interference
OSA	Optical Spectrum Analyser
P	Polarizer
PC	Polarization Controller
PPR	Positive Photoresist
RIE	Reactive Ion Etching

SEM	Scanning Electron Microscope
SOI	Silicon On Insulator
SWG	Straight Waveguide
TE	Transverse Electric
TIR	Total Internal Reflection
TLS	Tunable Laser Source
TM	Transverse Magnetic
UV	Ultra Violet
WDM	Wavelength Division Multiplexing

Units

$\mu\text{m}/\text{min}$	micrometer per minute (etch rate)
dB	Decibel (logarithmic power or amplitude ratio)
dBm	Decibel milliWatts (logarithmic power)
m	meter (length)
mbar	milliBar (pressure)
min.	minute (time)
mTorr	milliTorr (pressure)
mW	milliWatt (power)
mW/cm²	milliWatt per square centimeter (UV light intensity)
rpm	revolutions per minute (frequency of rotation)
sccm	standard cubic centimeter per minute (gas-flow rate)

Chemical Names

Ar	Argon
CHF₃	Trifluoro Methane
Cr	Chromium
H₂O₂	Hydrogen Peroxide
HF	Hydrofluoric Acid
IPA	Isopropyl Alcohol
NaOH	Sodium Hydroxide
SF₆	Sulphur Hexafluoride

Si	Silicon
SiO₂	Silicon Dioxide
TCE	Trichloroethylene

NOTATION

α	Waveguide loss
β	Propagation constant
β_n	Propagation constant of n^{th} mode
$\Delta\beta$	Phase mismatch
ϵ	Permittivity
ϵ_0	Vacuum permittivity
$\Delta\epsilon$	Permittivity of perturbation
ζ	Intensity contrast in Fabry-Perot response
θ_p	Angle of inclination of phase vector of p^{th} mode with respect to the waveguide axis
κ_m	Coupling coefficient between forward and backward propagating modes of single mode waveguide due to m^{th} Fourier coefficient of the periodic perturbation
λ	Wavelength
Λ	Grating period
λ_B	Bragg wavelength (phase matched for reflection)
λ_0	Phase matched wavelength in a grating structure
λ_m	Phase matched wavelength due to m^{th} order diffraction
ϕ	Phase change introduced upon total internal reflection
ω	Angular frequency
A_n	Weightage factor of n^{th} mode in the electric field distribution in a Waveguide
c	Velocity of light in free space
C_m	Component of κ_m that depends on the Fourier coefficient of the periodic perturbation
E	Electric field (distribution of a mode)
$\mathcal{F}_m[s]$	m^{th} Fourier coefficient of the periodic function s
G	Magnitude of grating vector
H	Rib height
h	Slab height
I	Overlap integral between the modes
I_{max}	Maximum output intensity
I_{min}	Minimum output intensity
k	Propagation constant (inside a medium)
k_0	Propagation constant (free space)
L	Grating length
m	Order of diffraction or index of Fourier coefficient
n	Refractive index

n_{clad}	Refractive index of waveguide cladding
n_{eff}	Effective refractive index of a waveguide mode
$n_{eff(q)}$	Effective refractive index of q^{th} mode of a waveguide
n_{Si}	Refractive index of silicon
n_{SiO_2}	Refractive index of silicon dioxide
p	Duty cycle
R	Reflection coefficient
R_{FP}	Reflectivity at the Fabry-Perot end facet
R_{max}	Maximum reflectivity
s	Periodic function representing the shape of the grating
T	Transmission coefficient
t	Thickness of planar dielectric waveguide
t_{max}	Maximum thickness of planar dielectric waveguide satisfying single mode condition
W	Rib width

CHAPTER 1

INTRODUCTION

1.1 Motivation

The progress in the area of photonics over the past few decades have opened a wide range of possibilities in the development of communication [1, 2] and sensing [3, 4] devices. Many of these devices are based on fiber optic and integrated optic components because these components offer high sensitivity and lower footprint at cheaper costs [5, 6]. Recently, there have been huge investments in the development and production of integrated optical components [7, 8, 9]. Periodic structures or gratings (especially, distributed Bragg reflectors) play major role in the realization of many of these devices.

In general, an optical grating or a periodic structure has periodic variation of refractive index in the medium, causing diffraction of waves interacting with them. As diffraction is a wavelength dependent phenomenon, the gratings have a wavelength dependent reflection and transmission spectra. This has led to a wide usage of such structures in communication, spectroscopy and sensing applications. Grating structures inscribed in fibers and waveguides (integrated optics) are widely used as distributed Bragg reflector (DBR) for wavelength selective operations. Fig 1.1 shows the schematic of a typical DBR grating structure. In DBR structures, the grating periodicity is typically chosen such that diffraction of electromagnetic waves in a band of wavelength (around λ_B) results in reflection. The Bragg wavelength, λ_B is defined by,

$$\lambda_B = \frac{2n_{eff}\Lambda}{m} \quad (1.1)$$

where n_{eff} is the effective index of a guided mode in the waveguide, Λ is the period of the grating and m is the order of diffraction.

Besides filtering [10], DBRs are also used as an integrated optical component to develop laser cavity, resonator, in-line delay, add-drop multiplexer, distributed feedback elements [11], wavelength switches [12] and chemical sensors [13]. Recently, they are also used in applications such as optical signal processing [14], and generation of slow light [15].

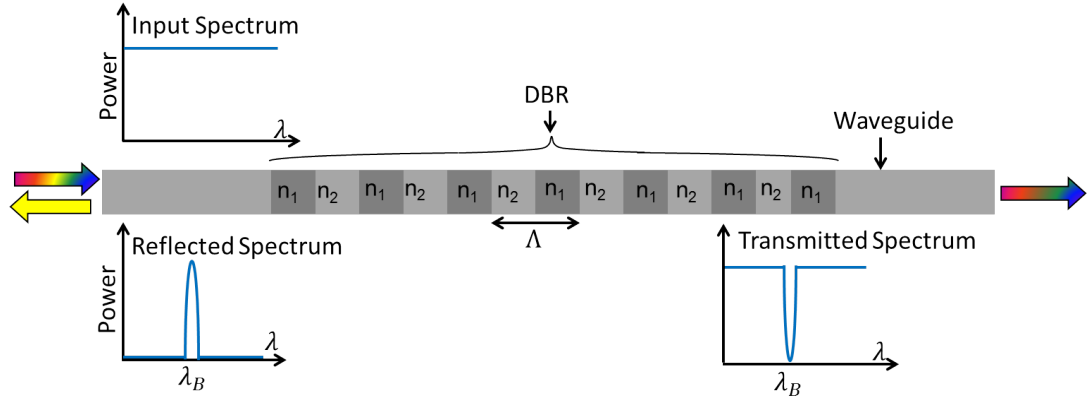


Figure 1.1: Schematic diagram of a distributed Bragg reflector (DBR). The periodic refractive index variation results in the reflection of the phase-matched wavelength (λ_B). Λ is the period of the DBR. Here, refractive indices n_1 and n_2 are used alternatively to represent the DBR structure.

Among various platforms for the fabrication of DBR, Silicon-on-Insulator (SOI) is adopted in the present work. The SOI platform has advantages like compatibility with well-established CMOS technologies and prospects of optical interconnects in place of conventional electrical interconnects. Besides, some SOI based integrated optical devices like straight and bend waveguides [16], directional couplers [17], MMI based power splitters [18], polarizers [19], interleavers [20], ring resonators and modulators [21] have been demonstrated by our integrated optoelectronics group. Considering the advantages of SOI based devices and the familiarity with the processes involved in the fabrication of SOI based devices, we have been motivated to design and fabricate integrated optical DBR structures in SOI platform.

DBRs in SOI platform were demonstrated in the past in four different geometries as shown in Fig. 1.2. The method that was initially developed and used most commonly is to make surface corrugations on top of the waveguides [22]. In order to allow more tolerance in the lateral misalignment between waveguide and gratings, Heimala et.al. [23] have demonstrated grating structures with corrugations

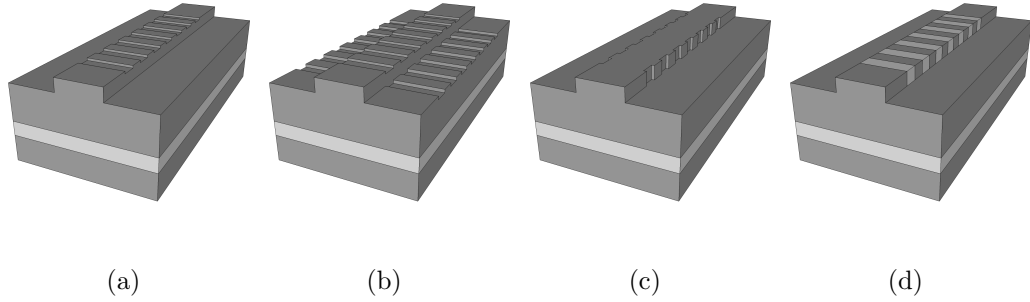


Figure 1.2: Various geometries of DBRs in SOI platform: (a) Surface corrugation in rib structure, (b) Surface corrugations in rib and slab, (c) Sidewall corrugations, (d) Implantation of oxide or defect inside the volume of the waveguide.

both in the top of the rib and in the slabs adjacent to them. There were also DBRs realized with periodically corrugated sidewalls [24]. This method requires only a single mask process for the realization of DBRs as well as waveguides. Another method for the realization of DBRs is by the periodic ion implantation of oxygen or silicon [25]. Unlike the other fabrication methods, this method maintains the planarity of the wafer surface which makes it easier for further processing. Typical values of maximum reflectivity, propagation loss and 3-dB bandwidth of a typical DBR structure (as in [26] fabricated using deep UV technology) are 12 dB, 0.28 dB/mm and 0.7 nm respectively.

Most of the DBRs demonstrated so far in SOI platform were designed with 1st order grating diffraction. However, eqn. 1.1 suggests that a period in the range of 224 nm is required for these devices to operate in C+L band (1520 nm to 1620 nm) when first order ($m = 1$) diffraction is used. Usually sophisticated techniques like electron beam lithography, deep UV lithography, focused ion-beam milling and ion implantation are used for the fabrication of such structures. These techniques require stringent fabrication control and result in low levels of yields.

The above mentioned limitations can be overcome by an appropriately designed higher order grating structure. Referring to eqn. 1.1, a choice of larger m would result in a larger required value of Λ for a reflection band in the C+L band. This principle can also be explained based on the Fourier decomposition of the refractive index profile. According to this, a sinusoidal gratings has only a single

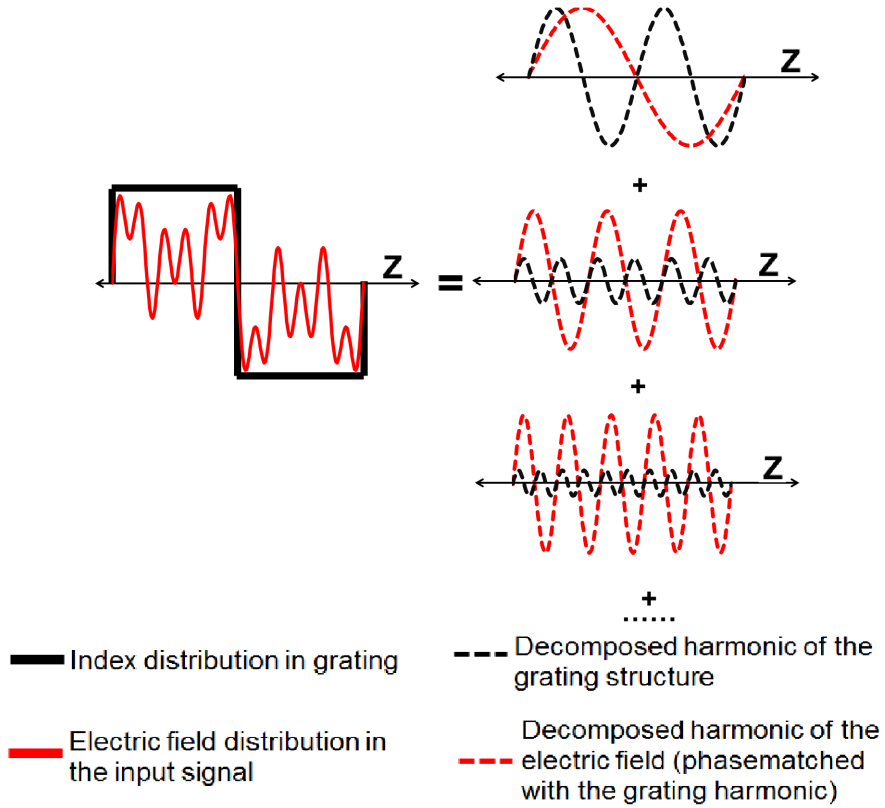


Figure 1.3: Schematic representation of phase matching due to higher order diffraction in a DBR. Solid black lines in the left side indicate the spatial distribution of refractive index in one of the periods of a hypothetical rectangular-grating. Solid red lines in the left side indicate the electric field distribution of an arbitrary input signal. Dashed black lines in the right side are the spatial harmonic components of the rectangular grating and the dashed red lines in the right side are the components of the signal which are phase matched and reflected due to the corresponding grating harmonic.

component in its spatial harmonics and its reflection peak is around a single wavelength ($\lambda_B = 2n_{eff}\Lambda$) [27]. Abrupt and periodic refractive index variations in a waveguiding medium has higher order spatial harmonics. The strength of the m^{th} harmonic depends on the shape of the fabricated structure and is proportional to the m^{th} coefficient in the Fourier series expansion of the periodic structure. These higher order spatial harmonics could be considered as sinusoidal refractive index variations with periods smaller than that of the fundamental period. Hence, they can be used to phase match wavelengths, smaller than those phase matched with the fundamental period.

As shown in Fig. 1.3, the refractive index profile in a DBR structure can

be considered as a combination of different spatial frequencies with appropriate weights, depending on the exact shape of the grating. The shape of a rectangular grating and its harmonic components are shown as solid black lines and dashed black lines, respectively. The frequency component of the input signal which gets phase matched to a given Fourier component of the grating gets reflected. Hence, for that frequency component of the input signal, the grating acts as a reflector. An arbitrary input signal and its Fourier components that are phase matched with the grating harmonics in case of Bragg reflection are shown as solid red lines and dashed red lines, respectively. By designing the grating to work at an appropriate higher order, we can avoid the requirement of smaller feature size.

1.2 Research Objective

Initially, the single mode waveguides as well as Bragg gratings have to be designed. While designing the devices, minimum feature size have to be chosen such that they are realizable with the facilities commonly available in microelectronics laboratories. The constraints of i-line (365 nm) photolithography and other fabrication processes limits the resolution of fabrication to feature sizes larger than $1 \mu\text{m}$. Hence, the objective of this work is to design, fabricate and characterize Bragg grating structures in single mode waveguides with periodicities $> 2 \mu\text{m}$ (smallest feature size $> 1 \mu\text{m}$) for acting as an efficient wavelength filter at $\sim 1.55 \mu\text{m}$.

1.3 Thesis Organization

Chapter 2 explores the theory and design aspects of single mode waveguide and Bragg reflectors. The conditions required for phase matching are explained based on phase diagrams. This chapter also provides an overview of the effect of various parameters of waveguide and gratings on the performance of Bragg reflectors. In the end, the optimized design parameters are summarized.

Chapter 3 presents the fabrication process and characterization of the DBRs.

Various processes involved in the fabrication and their optimized parameters are also discussed. Surface profiles of the fabricated structures and results of optical characterizations are analyzed in this chapter. The detailed description of the working devices are enlisted at the end of this chapter.

Finally, Chapter 4 summarizes the results of this research work and presents some of the future perspective of DBRs.

CHAPTER 2

BACKGROUND THEORY AND DESIGN

In this chapter, we present theoretical background and design parameters for DBR structures to be inscribed in single-mode rib waveguides in Silicon-on-Insulator (SOI) platform. The design parameters are optimized in accordance with the fabrication facilities commonly available in microelectronics laboratories. The effect of various parameters of waveguides and gratings on the performance of Bragg reflectors are analyzed. Finally, the desired dimensions of the waveguides and gratings are summarized.

2.1 Waveguide and Guided Modes

Waveguides are the fundamental components for integrated optical devices. In this work, waveguides are fabricated on the device layer of SOI wafers. The waveguides are chosen to be of rib geometry and large cross-section because of its lower coupling loss with the fiber [16]. Before moving on to the design of single mode rib waveguides in SOI platform, we start with a discussion of waveguiding in planar waveguides. Concept of phase diagrams is used to understand guided modes and condition for single-mode guiding. In the subsequent sections this concept is extended to explain phase matching and distributed Bragg reflection.

2.1.1 Phase Diagram of Planar SOI Waveguide

A monochromatic electromagnetic wave in free-space can be characterized by its phase vector which represents the direction of propagation and the magnitude of the phase constant. The the phase constant, k_0 is given by:

$$k_0 = \frac{2\pi}{\lambda_0} \tag{2.1}$$

where λ_0 is the free space wavelength.

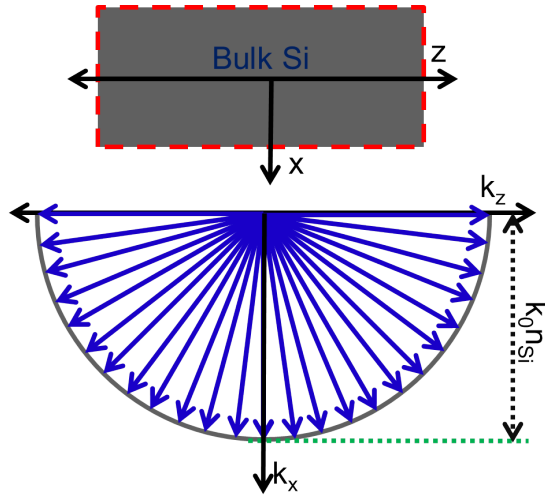


Figure 2.1: Phase diagram of a monochromatic wave with a wavelength λ_0 propagating in bulk silicon (with refractive index n_{Si}).

Inside a medium, wavelength is reduced by a factor n , where n is the refractive index of the medium. Correspondingly, the phase constant will have an increased magnitude, k given by

$$k = k_0 n = \frac{2\pi n}{\lambda_0} \quad (2.2)$$

In free space as well as in any unbounded medium, the wave can propagate in all the directions keeping the wavelength constant. This is equivalent in saying that within a medium, the phase vectors can be in any direction keeping its length constant. Hence, as shown in Fig. 2.1, in bulk silicon (with refractive index n_{Si}) the tips of the phase vectors of length $k_0 n_{Si}$ form a circle. The upper semicircle is not shown because of its redundancy.

The top part of Fig. 2.2 shows the cross section of a multimode slab waveguide in SOI platform. In this structure, the electromagnetic waves are confined to propagate in z direction. In contrast with the propagation in a bulk medium, inside a waveguide, waves can propagate only in discrete angles, θ_q satisfying the vertical standing wave relation [28] given by

$$2k_0 n_{Si} t \sin\theta_q - \phi_u - \phi_l = 2q\pi; \quad q = 0, 1, 2, \dots \quad (2.3)$$

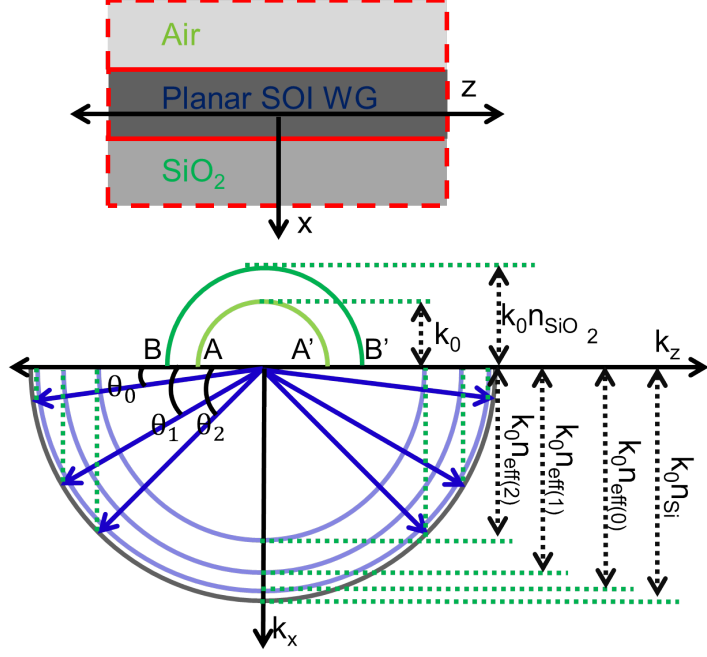


Figure 2.2: Phase diagram of a monochromatic wave with a wavelength λ_0 propagating in a multimode planar waveguide in SOI substrate.

where k_0 is the phase constant of the wave in freespace, n_{Si} is the refractive index of Si (hence k_0n_{Si} forms the phase constant inside Si). t is the thickness of the waveguide, θ_q is the angle of propagation. ϕ_u and ϕ_l are the phase changes introduced by the upper and lower waveguide boundaries on the reflected wave. In case of TE polarization, it is given by

$$\phi_{u,l} = 2 \tan^{-1} \frac{\sqrt{\cos^2 \theta_q - \left(\frac{n_{clad}}{n_{Si}}\right)^2}}{\cos \theta_q} \quad (2.4)$$

where n_{clad} is the refractive index of the cladding layer. Here, it takes the values 1 or n_{SiO_2} (refractive index of the bottom SiO_2 layer) depending on the reflection at upper and lower interfaces, respectively. A detailed derivation can be obtained in [28].

Hence, as shown in Fig. 2.2, in a multimode waveguide the phase vectors can have only discrete angles with respect to z axis. Each of these angles corresponds to a mode of this planar waveguide. We define the effective index of the q^{th} mode as $n_{eff(q)}$ where $k_0n_{eff(q)} (= k_0n_{Si}\cos\theta_q)$ is the projection of the q^{th} phase vector

along the waveguide axis. Consequently, this sets the upper limit of the effective index, as $n_{eff(q)} < n_{Si}$, which in physical sense is the limitation by the material medium of the waveguide core.

The lower limit of the the effective index of a propagating mode is set by the medium of the waveguide cladding. Propagation, if any, in the top air cladding and bottom SiO₂ cladding will be similar to bulk propagation. Hence, similar to Fig. 2.1, the tips of phase vectors in air and SiO₂ claddings form continuous circles. They are represented by the light green and dark green semicircles, respectively in Fig. 2.3. Hence, they will have an z component in the segment B-B'. As soon as the z-component of a mode reaches this limit, propagation through cladding is possible and the mode leaks out . This sets the minimum value for effective index as, $n_{eff(q)} > n_{SiO_2}$. Similarly, if we are able to make the z-component of a mode to lie in the A-A' segment, the wave leaks out to both SiO₂ and air substrates [29].

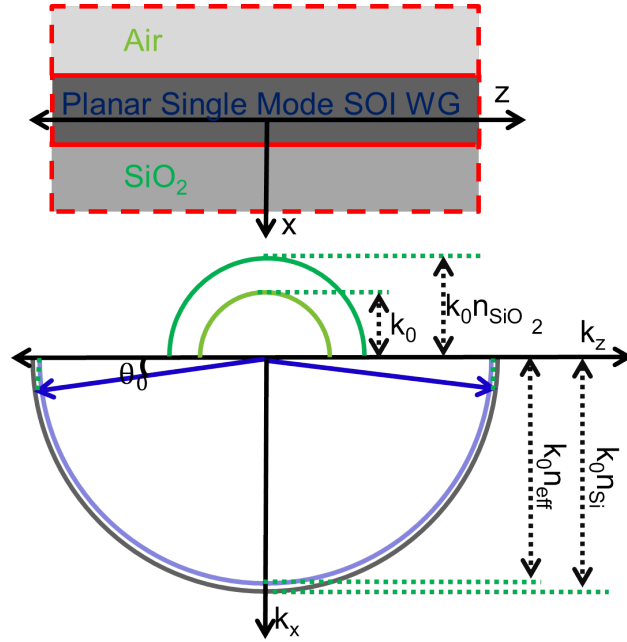


Figure 2.3: Phase diagram of a monochromatic wave with a wavelength λ_0 propagating in a single mode straight waveguide. n_{eff} is the effective index of the guided mode in the waveguide. k_0 is the phase constant in freespace. Hence, $k_0n_{SiO_2}$, k_0n_{Si} and k_0n_{eff} are the phase constants in the SiO₂, Si and Si singlemode waveguide.

Further, restricting the dimensions of the waveguides to satisfy single mode condition results in supporting only a unique angle, θ_0 for the phase vectors with

respect to the waveguide axis. Thus, as shown in Fig. 2.3, in a single mode waveguide only two counter propagating modes with the same effective index are possible. They both have the same effective index, and is represented as n_{eff} . In case of a planar waveguide formed on a specific substrate, the single mode condition at a wavelength is obtained by restricting the height, t of the waveguide within a maximum value t_{max} that can be derived from eqn. 2.3. In case of a rib waveguide, the confinement is two dimensional and the single mode condition is obtained by simultaneous design of all the lateral dimensions of the waveguide.

2.1.2 Design of Single Mode Rib Waveguides

Fig. 2.4 shows the schematic of a typical rib waveguide fabricated on a SOI wafer. Waveguiding in this structure is by the material and structural properties. The buried oxide layer at the bottom and air at the top act as the claddings for these waveguides. As the refractive index of these claddings are lower than that of silicon, light is confined in the x direction due to total internal reflection at the interfaces of these claddings. Along the the y direction, confinement is due to the effective index change arising from the rib structure.

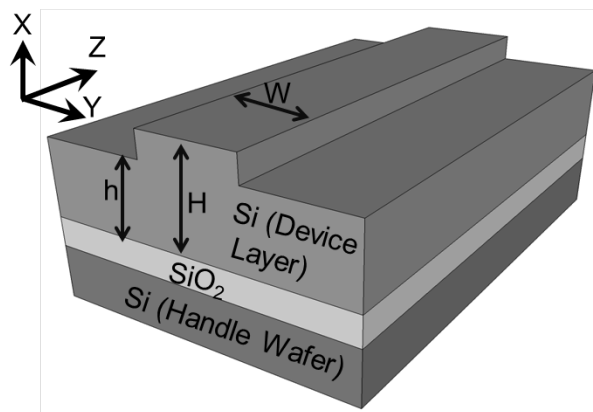


Figure 2.4: Schematic view of a large cross-section rib waveguide. Typical values for single mode waveguiding: $H = 5 \mu\text{m}$, $h \sim 3.8 \mu\text{m}$, $W \sim 5 \mu\text{m}$. Fundamental mode size is comparable to standard single mode fiber.

In this current work, as we are interested in the operation of our device at C+L bands of communication wavelengths, we chose to design our single mode waveguides at around 1550 nm. The design and analysis of rib structures includes

the calculation of their effective index, single mode dimensions and mode profiles at the wavelengths of interest. These analysis are done exactly by solving the Maxwell's equations. However, it is challenging to obtain analytical solutions, except for some standard waveguide geometries. Hence a series of approximations and simplified approaches are being followed. One of the popular approximation is by neglecting the field components in the propagation direction and reducing the vector Maxwell's equation into two independent sets of scalar equations. The solutions of these sets of equations can be classified as the TE modes and TM modes, depending upon the orientation of major field components. With reference to Fig. 2.4 these modes have the electric field along y and x directions, respectively. As these two modes satisfy different sets of equations and can be treated independently, we chose to concentrate our design for TE polarization. The design of a rib geometry as shown in Fig. 2.4 constitutes the specification of the rib height, H , the slab height, h and the width, W of the waveguide.

As the SOI wafers are procured commercially, they are obtained with standard device layer thicknesses. A device layer thickness of $5 \mu\text{m}$ is usually used for the fabrication of large cross section devices. Accordingly, the rib height, H was chosen to be $5 \mu\text{m}$. With this as the initial criterion, the design of the waveguides are done by considering single mode operation, fabrication limitations and losses, in the following sequence.

1) Choice of waveguide parameters for single-mode guiding:

After the realization of waveguides, DBRs have to be incorporated onto them. Hence, single mode condition have to be maintained in the waveguide design in order to avoid cluttered multiple peaks in the DBR response. In case of multimode waveguides, the multiple peaks occur in the DBR response because of the closely spaced effective indices of the modes. It can be shown using eqn. 1.1 that, in a multimode waveguide, closely spaced multiple wavelengths will get reflected.

There have been many approaches for obtaining the single mode condition in a rib structure. This include both analytical approaches like effective index [30, 31]

and weighted index methods as well as numerical methods like finite element [32] and finite difference analysis [33]. In this work, the effective index method is used because this method is quite accurate for our case of large slab height [34]. Moreover, the error in effective index method is positive, keeping the single mode limit safer in case of fabrication tolerances. Using effective index method, the rib structure is analyzed by decomposing it into three planar waveguiding structures. The possible dimensions of waveguide width, W and slab height h , for a rib height, $H = 5 \mu\text{m}$ to ensure single mode operation are calculated using the effective index method. As shown in Fig. 2.5, these dimensions are demarcated using the solid line and the hatched region below it. The detailed analysis of this approach is given in [28, 35].

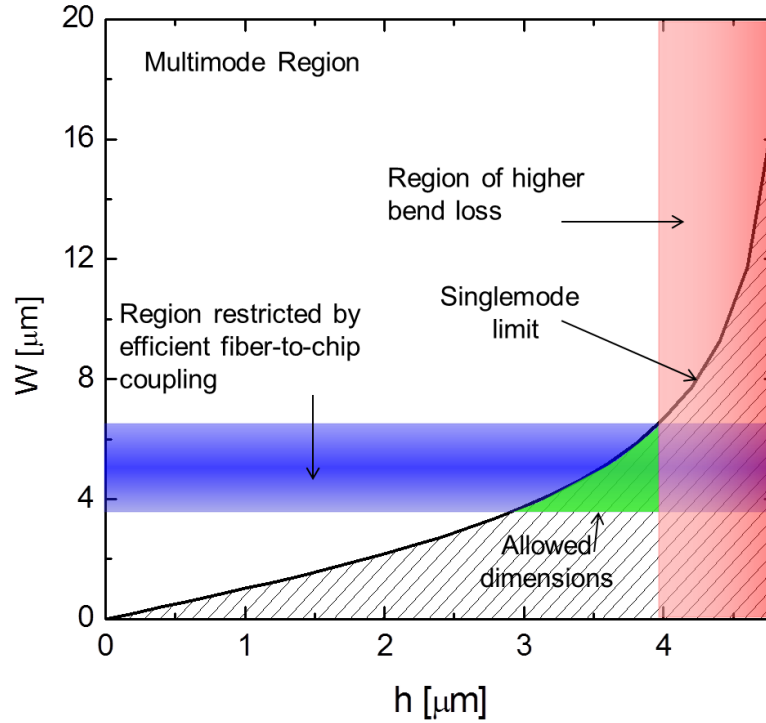


Figure 2.5: Graphical representation of choosing waveguide parameters for a SOI device layer thickness of $5 \mu\text{m}$. The dimensions satisfying single mode condition (at wavelength, $\lambda \sim 1550 \text{ nm}$.) are demarcated using the solid black line and the hatched region below it. Dimensions with larger slab heights (red) are avoided due to increased bend losses. Waveguide widths in the blue region are preferred for efficient fiber-chip coupling. The allowed dimensions are indicated in green colour.

2) Restrictions to minimize the fiber-to-chip coupling loss:

Integrated optical devices are usually coupled with optical fibers in order to transfer light into and out of these devices. Hence, the modes of the fiber and the device must be similar in order to have a minimum coupling loss. As the waveguide height, H is $5 \mu\text{m}$, the waveguide width, W has to be $\sim 5 \mu\text{m}$ in order to match with the circular symmetry of the fiber mode profile. Thus the waveguide width was chosen such that $3.5 \mu\text{m} < W < 5.5 \mu\text{m}$. Correspondingly, the desired regions are shown in blue in Fig. 2.5.

3) Further restricting the dimensions considering the application related criteria:

Larger slab heights results in lesser confinement of light in the rib region and it results in the increased bend losses. This is relevant because in most of the potential applications, DBRs are incorporated in structures having many bends. The region to be avoided is shown in red. Thus the allowed dimensions that satisfy all the above constraints are indicated by green, in Fig. 2.5.

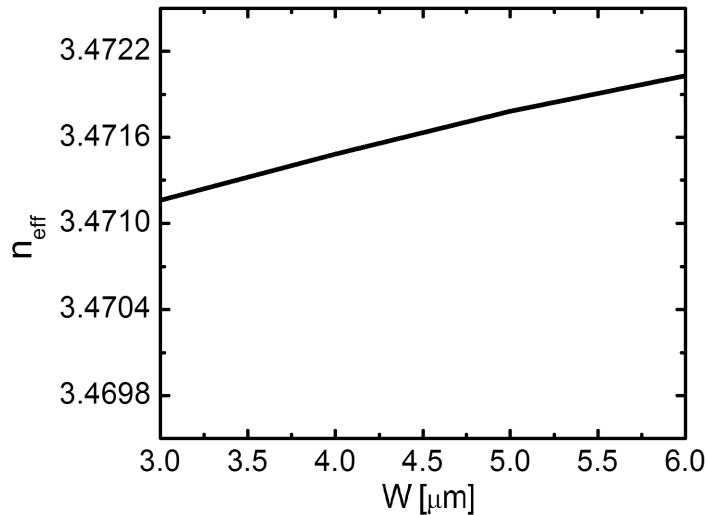


Figure 2.6: Effective index of TE modes in the rib waveguide with $H = 5 \mu\text{m}$, $h = 3.8 \mu\text{m}$ for $\lambda = 1550 \text{ nm}$.

According to the above considerations, the waveguide widths of the fabricated devices are varied from $3.5 \mu\text{m}$ to $5.5 \mu\text{m}$ in steps on $0.5 \mu\text{m}$ while keeping rib height, H as $5 \mu\text{m}$ and slab height, h as $3.8 \mu\text{m}$.

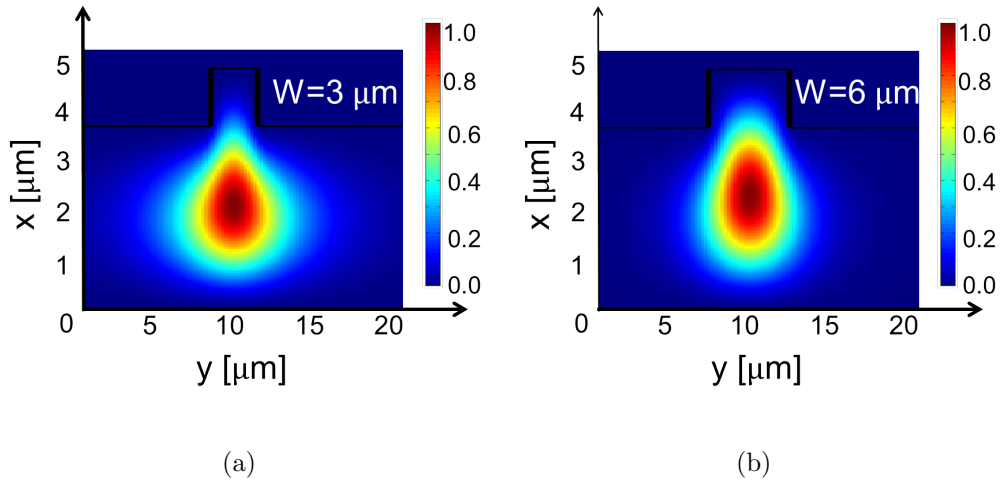


Figure 2.7: The typical mode profiles for (a) $W=3 \mu\text{m}$ and (b) $W=6 \mu\text{m}$ for TE polarization obtained using RSOFT MODE SolutionsTM. As the waveguide width increases, the mode gets more confined in the rib region.

Using a commercial simulator RSOFT MODE SolutionsTM, mode profiles as well as the effective refractive index in the waveguiding structures are obtained. It is a full-vectorial mode solver based on finite element algorithm [36]. The effective indices as a function of waveguide width, W is shown in Fig. 2.6. The effective index is required in estimating the phase matched wavelength (eqn. 1.1). The mode profiles for two of the waveguide widths, $W = 3 \mu\text{m}$ and $W = 6 \mu\text{m}$ are shown in Fig. 2.7. The mode profiles of the gratings are important to calculate the grating efficiency as in Section. 2.2.2. With the understanding of phase diagrams as well as with the single mode dimensions, mode profiles and effective refractive indices of the waveguides, we moved on to the design of DBR structures.

2.2 DBRs in Single Mode Rib Waveguides

In this section, the Bragg reflectors on a planar single mode waveguide is analysed in terms of phase diagrams. This gives a qualitative background of phase matching. The exact quantitative formula using coupled mode theory is discussed in the further subsections. This is used for the calculation of reflection spectrum of DBRs in a rib structure.

2.2.1 Phase Diagram of DBR in Single Mode Planar Waveguide

In this section, the phase matching in DBRs is discussed, based on the phase diagrams. The variations in phase diagrams of a single mode slab waveguide (section. 2.1.1) upon the introduction of DBRs is discussed. The concept of grating vector and phase mismatching due to DBRs are also introduced in this section.

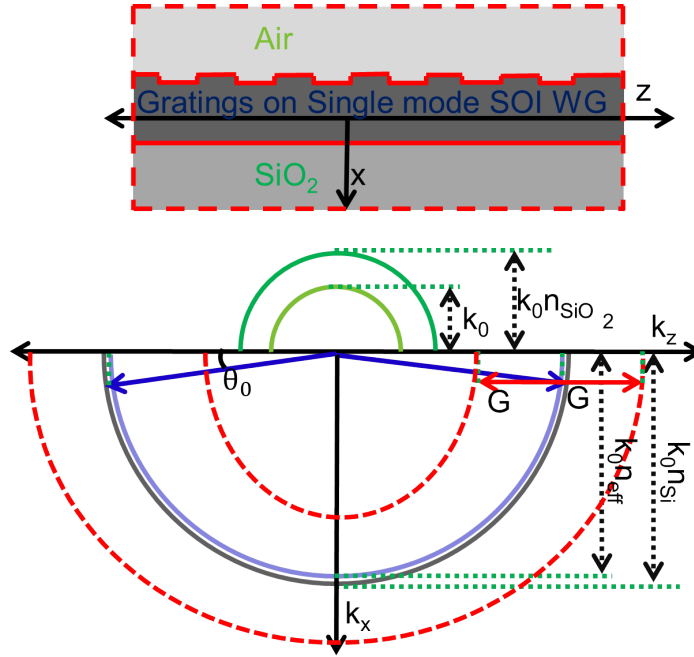


Figure 2.8: Phase diagram of a monochromatic wave with a wavelength λ_0 propagating in a single mode waveguide (see Fig. 2.3) with gratings.

Discontinuities in a waveguide causes reflection of the electromagnetic waves. If there are multiple discontinuities, the different components of the wave reflected from the different discontinuities interfere depending on the phase relations between them. The phase relations in turn depend on the path difference between the components. In case of a grating, the discontinuities are periodic and hence the path difference between successive reflections are same. The scattered wave components have a constant phase difference and they interfere with each other, changing the component of the phase vector along the direction of periodicity (along z axis). This is indicated as the addition and subtraction of grating vector,

G defined as

$$G = m \frac{2\pi}{\Lambda} \quad (2.5)$$

from the z component of the phase vector on the waveguide mode. A detailed derivation of this is given in [37].

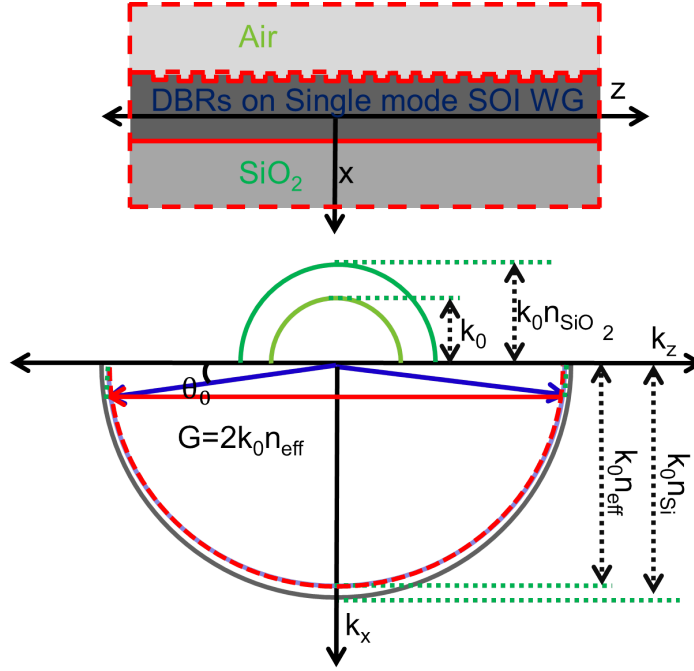


Figure 2.9: Phase diagram of a monochromatic wave with a wavelength λ_0 propagating in a single mode waveguide with DBRs. The wavelength λ_0 is phase matched with period of the DBR structure.

Fig. 2.8 shows a planar single mode waveguide with DBRs incorporated on them and corresponding phase diagram. Here, the grating vectors are added and subtracted with the z -component of the phase vector of the forward propagating mode. In this particular case, as the resultant vectors formed by the guided wave and grating vectors do not coincide with any allowed mode in the waveguide, they will not exist. But if we choose the period of the grating, Λ such that $G = 2k_0n_{eff}$, one of the resultant vectors coincide with the backward propagating mode as shown in Fig. 2.9. DBRs are such carefully designed gratings which reflects back the forward propagating mode.

For a fixed grating period, complete phase matching occurs at unique wavelength, λ_0 . But for any other wavelength, λ' and corresponding free space wave

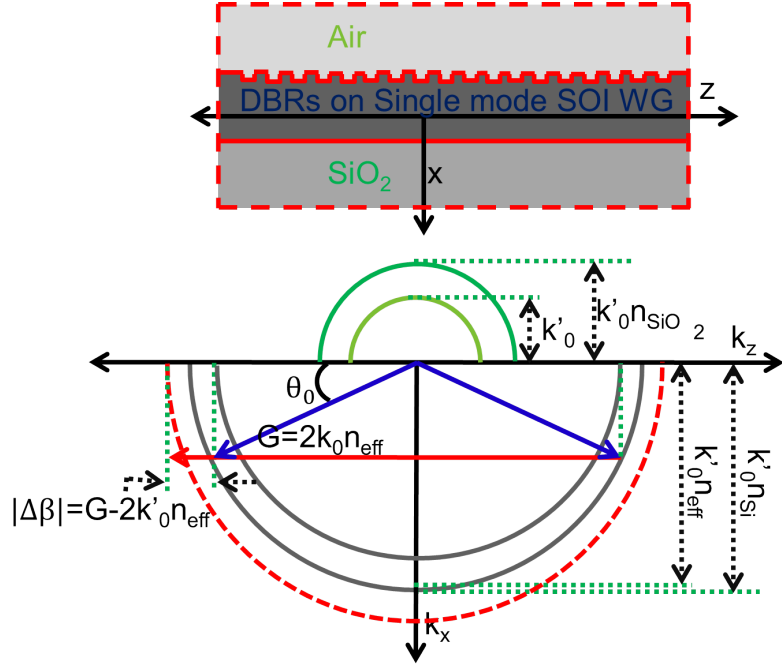


Figure 2.10: Phase diagram of a monochromatic wave with a wavelength λ' propagating in a single mode waveguide with DBRs. The wavelength λ' is not phase matched with period of the DBR structure.

vector k'_0 , the same grating structure will have a phase mismatch given by

$$\Delta\beta = 2k'_0n_{eff} - G \quad (2.6)$$

Fig. 2.10 shows the phase diagram of monochromatic waves with wavelengths $\lambda' \neq \lambda_0$. Corresponding to non-zero phase mismatch, the reflectivity gets reduced from the maximum possible value and the exact reflectivity, as a function of phase mismatch is given in the subsequent section.

2.2.2 Rib Waveguides with Higher Order DBR Structures

The design of DBR structure realized by the surface corrugation in large cross-section rib waveguides is carried out for TE Polarization, following the coupled mode analysis as proposed by Yariv [27].

Fig. 2.11 shows the structure used for the analysis. A comprehensive analysis of this structure is given in APPENDIX. A.1. The reflectance, R and transmittance,

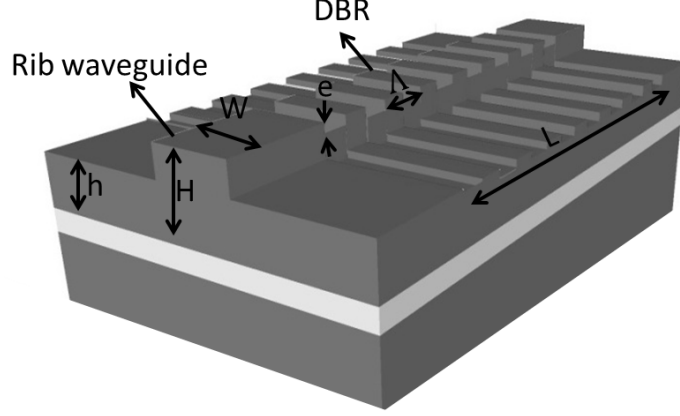


Figure 2.11: Schematic view of DBR structures on a large cross-section rib waveguide ($H = 5 \mu\text{m}$, $h \sim 3.8 \mu\text{m}$, $W \sim 5 \mu\text{m}$)

T of such a structure for TE polarization is given by

$$R = \frac{|\kappa_m|^2 \sinh^2(sL)}{s^2 \cosh^2(sL) + \left(\frac{\Delta\beta}{2}\right)^2 \sinh^2(sL)} \quad (2.7)$$

$$T = \frac{s^2}{s^2 \cosh^2(sL) + \left(\frac{\Delta\beta}{2}\right)^2 \sinh^2(sL)} \quad (2.8)$$

Here $\Delta\beta$ is the phase mismatch factor. s is defined as $s = \sqrt{|\kappa_m|^2 - \left(\frac{\Delta\beta}{2}\right)^2}$ and κ_m is the m^{th} order coupling coefficient between the forward and backward propagating modes in the waveguide, given by

$$\kappa_m = C_m I \quad (2.9)$$

where C_m is obtained from terms of m^{th} Fourier coefficient in the Fourier series expansion of the periodic structure. For DBRs with rectangular grooves, C_m is given by the expression

$$C_m = \frac{\omega}{4} \epsilon_0 (n_{eff}^2 - 1) \frac{\sin\left(\frac{m\pi}{2}\right)}{m\pi} e^{\frac{im\pi}{2}} \quad (2.10)$$

where ω is the angular frequency corresponding to the wavelength considered and n_{eff} is the effective index of the waveguiding structure for TE polarization. A more detailed analysis is presented in APPENDIX A.1.

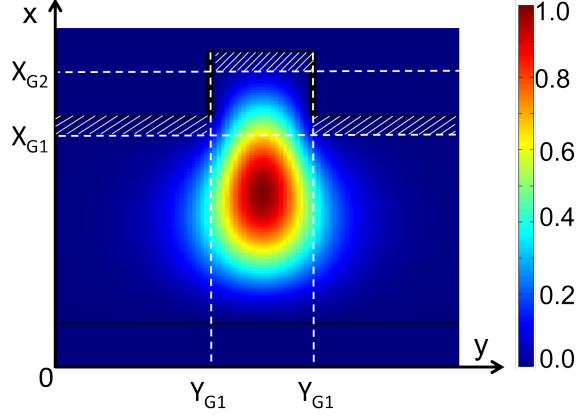


Figure 2.12: The mode profile (TE polarization) of a waveguide with the typical dimensions as given in Fig. 2.11 caption. Parts of the mode profile overlapped with etched grating structure is demarcated by hatching. X_{G1} , X_{G2} , Y_{G1} and Y_{G2} are the coordinates defining the limits of integration in the evaluation of overlap integral. The regions of integration are: (1) $X_{G1} < x < \infty$, $0 < y < Y_{G1}$, (2) $X_{G2} < x < \infty$, $Y_{G1} < y < Y_{G2}$ and (3) $X_{G1} < x < \infty$, $Y_{G2} < y < \infty$.

I given in eqn. 2.9 is the overlap integral between the normalized mode profiles of the forward propagating and backward propagating modes in the grating region. In case of the single mode waveguide, they are identical. The integrals are numerically evaluated from the mode profile, $E(x, y)$ of the waveguide obtained using RSOFTTM Mode solver. The profile, $E(x, y)$ is first normalized to $E_n(x, y)$ using the relation,

$$E_n(x, y) = \frac{E(x, y)}{\sqrt{\int_{-\infty}^{\infty} \int_{-\infty}^{\infty} E(x, y) dx dy}} \quad (2.11)$$

Using the normalized mode profile, for shallow-etched grating on a single mode waveguide, I is evaluated as

$$I = \int_{X_{G1}}^{\infty} \int_0^{Y_{G1}} |E_n(x, y)|^2 dx dy + \int_{X_{G2}}^{\infty} \int_{Y_{G1}}^{Y_{G2}} |E_n(x, y)|^2 dx dy + \int_{X_{G1}}^{\infty} \int_{Y_{G2}}^{\infty} |E_n(x, y)|^2 dx dy \quad (2.12)$$

The extracted mode profile with the limits of integration is shown in Fig. 2.12.

Waveguide parameters and the etch depth of gratings affect the DBR reflectiv-

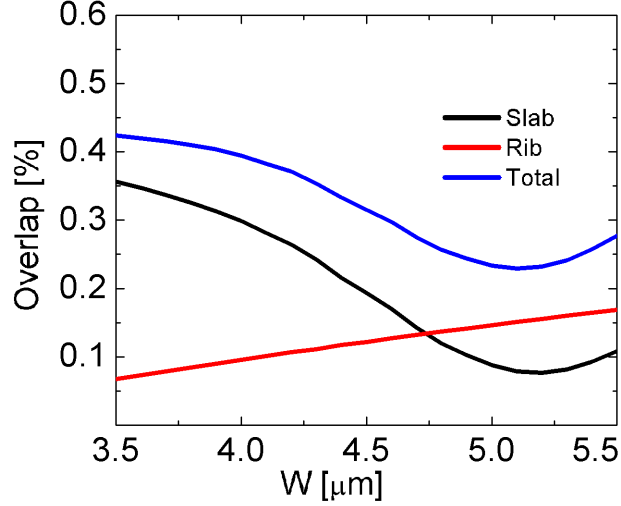


Figure 2.13: The variation of total overlap integral (blue) as a function of waveguide width, W . Overlap integral due to gratings in slab (black) and rib (red) regions are indicated separately.

ity because of the change in the overlap integral (I) in eqn. 2.12. A larger overlap integral corresponds to a larger coupling coefficient and hence a larger reflectivity. The variation of overlap integral as a function of waveguide width is shown in Fig. 2.13. The change in waveguide parameters changes the integrand i.e the mode profile $E(x, y)$; whereas change in grating etch depth changes the limits of integration - X_{G1} , X_{G2} , Y_{G1} and Y_{G2} . Thus, for a given waveguide parameters, the coupling coefficient generally increases with the grating etch depth whereas the variation is not monotonous with respect to other waveguide parameters.

2.2.3 Choice of Diffraction Order, Periodicity and Length

The criteria for deciding the period and order are:

1. The overall resolution for fabrication (minimum possible feature size $1 \mu\text{m}$ and correspondingly a grating period, $\Lambda > 2 \mu\text{m}$).
2. The operation of the device in the C+L band (1530 nm to 1620 nm).

Fig. 2.14(a) shows the variation of reflection as a function of phase matching. It is observed that the maximum reflection, R_{max} for a given DBR occurs at a wavelength corresponding to zero phase mismatch. For the design of order and period, phase mismatch for various orders of diffraction for $\Lambda > 2 \mu\text{m}$ is considered.

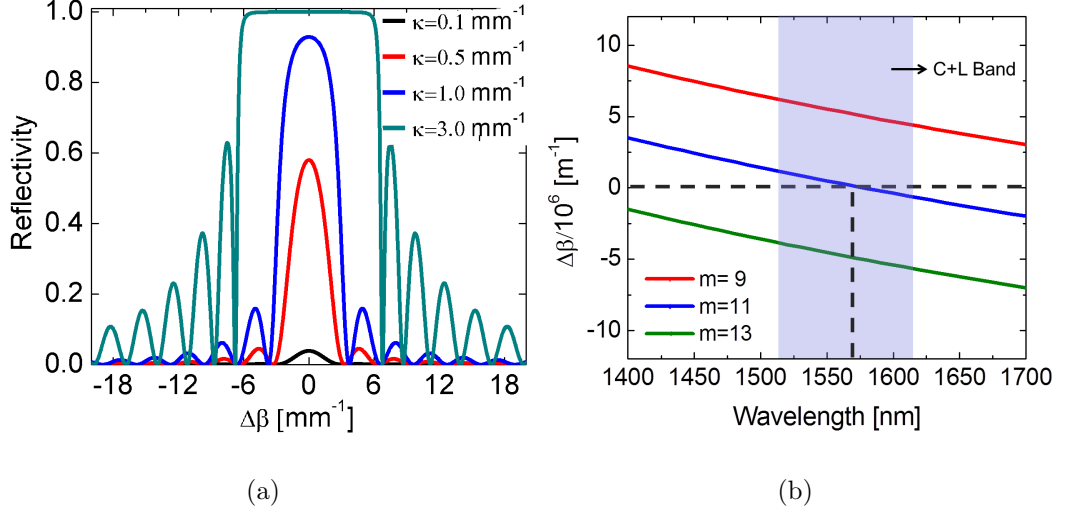


Figure 2.14: (a) Reflection spectrum as a function of phase matching, $\Delta\beta$ for some typical values of κ and a grating length of 2 mm. (b) Variation of $\Delta\beta(\lambda) = 2\beta_1 - m\frac{2\pi}{\Lambda}$ as a function of λ . The zero phase mismatch and hence the reflection peak for 11th order diffraction occurs at $\lambda_B \sim 1560$ nm for a grating period, $\Lambda = 2.5 \mu\text{m}$.

It is apparent from eqn. 1.1 that, in the designed dimensions of the waveguide ($n_{eff} \sim 3.47$), the minimum value of m is 11 in order to obtain $\Lambda > 2 \mu\text{m}$. For $m = 11$, the zero phase mismatch occurs in the C+L-band ($\lambda_B \sim 1560$ nm) for a grating period of $\Lambda = 2.5 \mu\text{m}$. This is shown in Fig. 2.14(b) by zero phase mismatch for $m = 11$ at $\lambda \sim 1560$ nm for $\Lambda = 2.5 \mu\text{m}$.

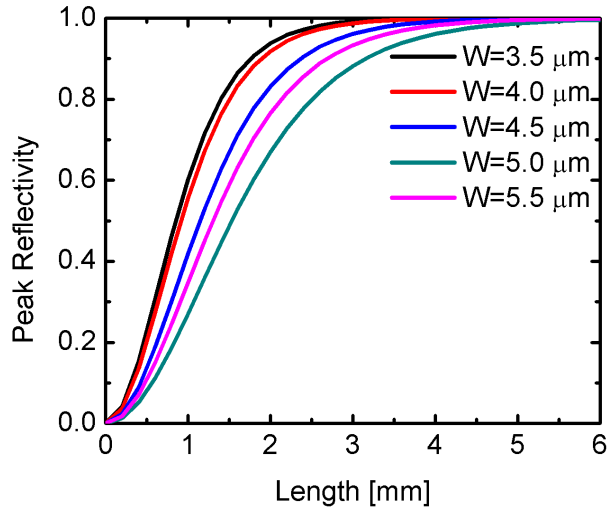


Figure 2.15: The variation of peak reflectivity as a function of grating length for various waveguide widths.

The peak reflectivity, R_{max} of a grating increases with the grating length. The typical variation of peak reflectivity as a function of grating length for various waveguide widths and 300 nm grating etch depth is given in Fig. 2.15. Accordingly a grating length of 3 mm is chosen so as to obtain a peak reflectivity > 0.9 .

2.2.4 Fabrication Tolerance to Design Parameters

The grooves of the gratings are typically modeled to have vertical walls. However, in a fabricated structure, perfect vertical nature may not be maintained. An extreme case of this is a triangular structure corresponding to an over-etched case. However, a typical possibility is that in which the rectangular regions in the gratings get deformed to trapezoidal structures with an inclination of 10° . The reflectivity for various orders for 50% duty cycle for rectangular profile, symmetric triangular profile and trapezoidal profile is depicted in Fig. 2.16. A comprehensive analysis of these structures as well as the dependence of reflectivity on shape of the grating are given in APPENDIX. A.1. It can also be seen from Fig. 2.16 that a 9th order grating will have a higher reflectivity and 13th order grating has a lower reflectivity, compared to 11th order grating.

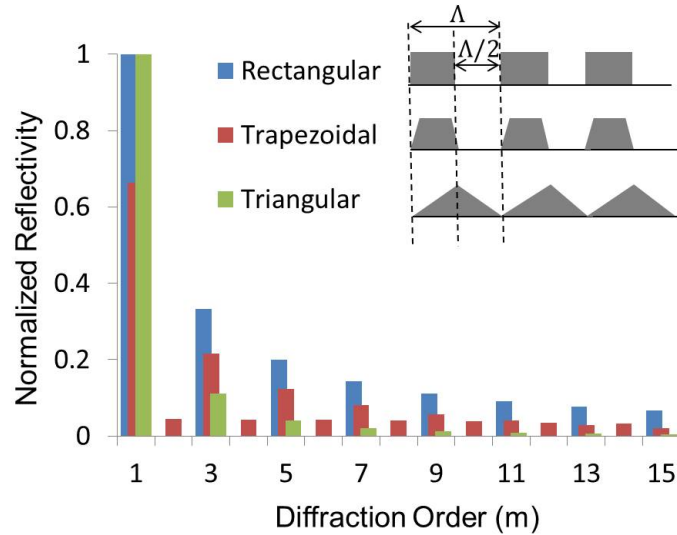


Figure 2.16: Normalized reflectivity corresponding to various diffraction orders for (i) rectangular gratings, (ii) trapezoidal gratings with an inclination 10° and (iii) symmetric triangular gratings.

The change in duty cycle can also change the reflectivity. This is attributed

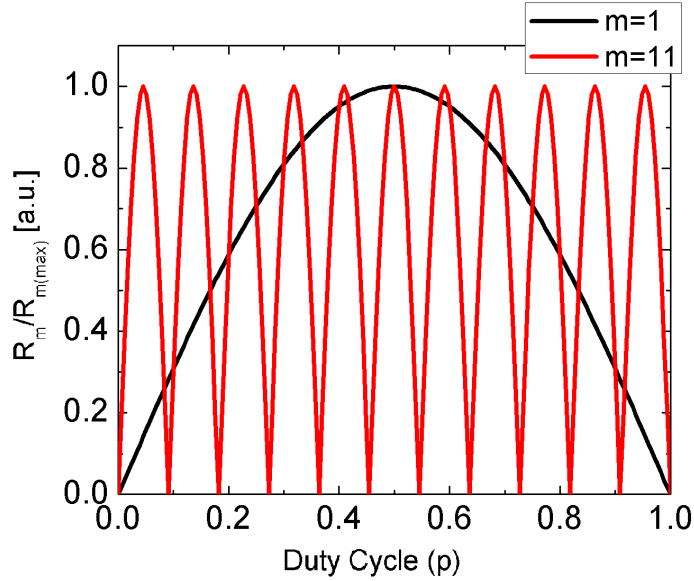


Figure 2.17: The variation of reflectivity for first order and 11th order rectangular gratings as a function of duty cycle (p). The reflectivities are in turn normalized to the maximum reflectivity in the corresponding orders.

to the change in the corresponding harmonic component of the grating. Variation of reflection coefficient as a function of dutycycle, p for a rectangular grating is shown in Fig. 2.17. It is evident from the graph that in a first order grating, the reflection coefficient drops down monotonically as the duty cycle deviates from 0.5. But in an 11th order gratings, the design is highly stringent. Maximum reflection is obtained when the duty cycle satisfies the condition $p = \frac{2n+1}{22}$ where $n = 0, 1, 2, \dots$ upto 10. A variation of 9.1 % in the duty cycle would result in a change of 100 % in the reflectivity, for $m = 11$. Similar to the above arguments, a 9th order grating, which require a smaller feature size (better fabrication resolution) will have a better fabrication tolerance whereas, a 13th order grating, which requires only a larger feature size will have a worse tolerance. Thus, there is a trade off between the smallest feature size and the achievable design tolerance in reflectivity.

2.2.5 Optimized Parameters

The important parameters for single-mode guiding and the DBR operating at $\lambda \sim 1550$ nm have been optimized based on coupled mode theory as discussed in previous section. In the theoretical analyses, it is assumed that the guided eigen

mode is weakly perturbed by the surface corrugated periodic structure with its 11th order Fourier coefficient. The final parameters (see Table 2.1) were optimized such that the device could be fabricated using conventional microelectronics fabrication facilities (1 μm technology).

Table 2.1: Optimized design parameters for integrated optical DBR structure with large cross-section rib waveguide structure.

Parameter	Symbol	Designed Value
Rib height	H	5.0 μm
Slab height	h	$\sim 3.8 \mu\text{m}$
Waveguide width	W	$\sim 3.5 \mu\text{m}$
Diffraction Order	m	11
Grating Period	Λ	$\sim 2.5 \mu\text{m}$
Duty Cycle	p	0.5
Grating Length	L	$\sim 3 \text{ mm}$

CHAPTER 3

FABRICATION AND CHARACTERIZATIONS

This chapter starts with an outline of the design and fabrication of optical masks. Then device fabrication processes and their optimized parameters are enlisted. Finally, the characterization procedure is discussed along with the results in loss measurement, mode profile and spectral response.

3.1 Optical Mask Design and Fabrication

Our fabrication approach for DBRs used photolithography and subsequent development and RIE to transfer the patterns onto the substrate. As two different levels of etching were required, two optical masks were used for the construction of DBRs. The first mask was used to defined the DBR patterns whereas the second mask was used to define the waveguide structure.

The mask layouts were created using R-softTM CAD tool [38]. The layout consisted of large number ($> 10^4$) of structural elements. In order to take into account the fabrication tolerances involved in the mask and device fabrication, the waveguide and grating parameters were required to be varied systematically around the designed values. Hence C programming code was used to generate the RSOFTE scripts defining the mask structure. The RSOFTE format for a typical mask element and c-codes used in the mask generation are given in APPENDIX. B.1 and APPENDIX. B.2, respectively.

The layout of the different masks are given in Fig. 3.1. The first mask consisted of grating patterns of five different periods - $2.3 \mu\text{m}$, $2.4 \mu\text{m}$, $2.5 \mu\text{m}$, $2.6 \mu\text{m}$ and $2.7 \mu\text{m}$ - and a few completely masked regions. Each of the grating periods constituted a block in the first mask and were wide enough to accommodate 5 straight waveguides of varying widths - $3.5 \mu\text{m}$, $4.0 \mu\text{m}$, $4.5 \mu\text{m}$, $5.0 \mu\text{m}$ and $5.5 \mu\text{m}$

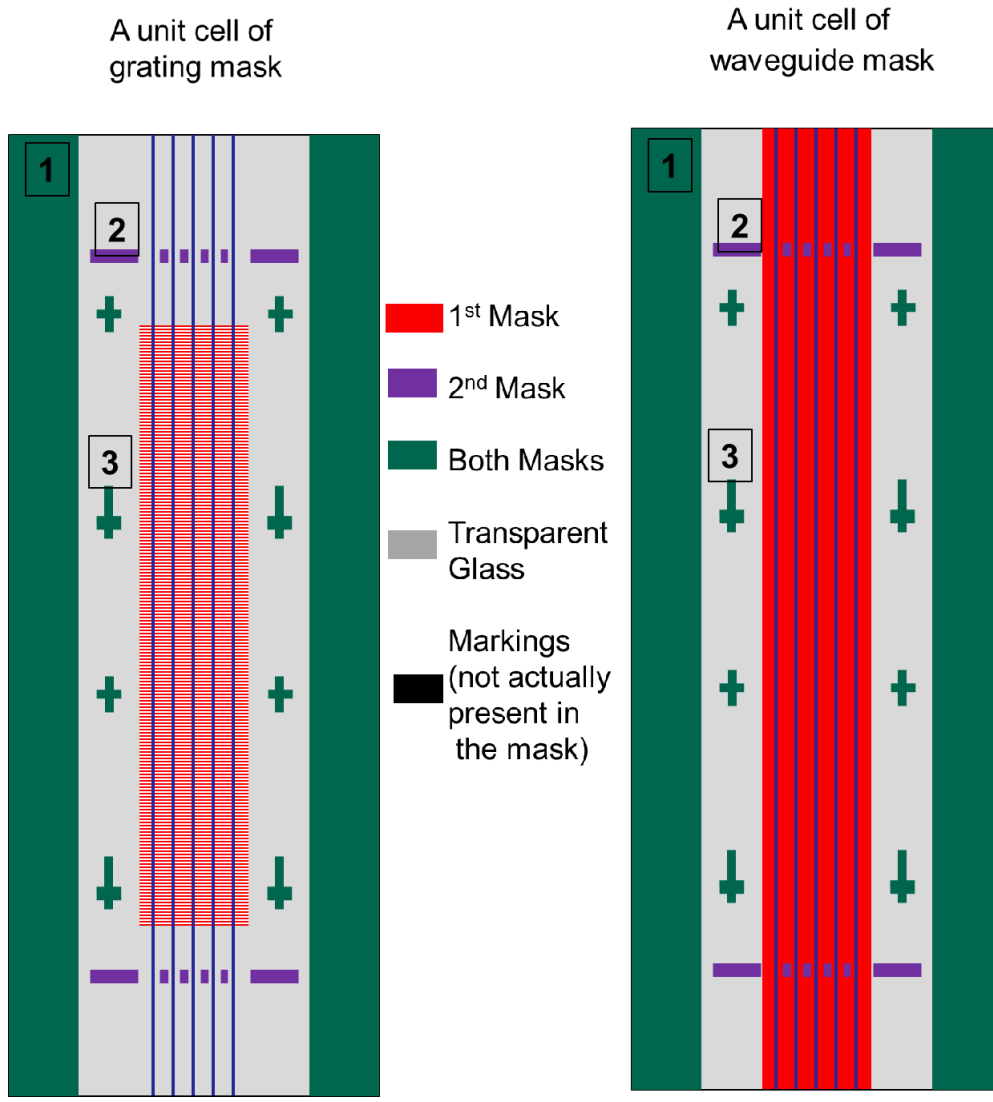


Figure 3.1: Mask layouts used for the fabrication of integrated optical DBR structures in SOI. Regions in the first mask (red), the second mask (violet) and both (green) are shown in different colors. The structures marked in the layout are (1) slab, (2) alignment markers and (3) polishing markers.

- in the second mask. The completely masked regions in the first mask were used to fabricate reference straight waveguides in the second mask.

In addition to the designed devices, slabs, alignment markers and polishing markers were included in the masks for various practical reasons.

1) **Slabs:** It is easier to couple light into and out of slab regions compared to the waveguides and other devices. Hence slabs were helpful in the alignment of samples during characterization. Also measurement of depth and verticality of

etching was easier in the slabs.

2) Alignment Markers: Angular as well as lateral alignment of the second mask with respect to the first mask was achieved by cross-shaped alignment markers. After the fabrication with the first mask, the alignment markers will be present in the sample. For the alignment of the second mask, the markers in the second mask were adjusted to overlap with the markers in the sample. For better accuracy, the alignment markers were made such that half of them were larger compared to the other half. Larger marks provided the initial alignment where as the precise alignment was achieved by the smaller marks.

3) Polishing markers: Polishing markers were included perpendicular to the waveguides. This was to provide a convenient method for polishing the sample edges perpendicular to the waveguides. The sample edges were made perpendicular to the waveguides by polishing the edges parallel to these polishing markers.

The patterns created in the RSOFTE were converted to the current standard photomask plotting format, Graphic Database System 2 (GDS2) format. The patterns were then transferred to the photoresist coating on the mask plate using our DWL66 ¹ writer. Specifications of the mask plate are given in Table. 3.1

Table 3.1: Specifications of the mask plate.

Transparent layer	: fused silica
Absorbing layer	: Chromium (~ 50 nm thick)
Photoresist	: AZP-1350 (~ 0.5 μ m thick)

Direct writing of the pattern was done and then the photoresist was developed using NaOH solution. Chromium development was done using the chrome etchant. Finally the remaining PPR was removed by cleaning with acetone and Piranha. The details of the chemistry are reported in APPENDIX C.

¹manufacturer: Heidelberg Instruments GmbHTM, laser source: He-Cd laser of $\lambda = 442$ nm

3.2 Process Optimization

It takes several iterations to perfect the fabrication sequence. Hence, initially the fabrication was carried out in silicon wafer which was cheaper than SOI. The specifications of the silicon and SOI wafers used are given in Table. 3.2 and Table. 3.3, respectively.

Table 3.2: Specifications of the silicon wafer used for optimizing the fabrication processes.

Doping	: P-type
Resistivity	: 1 – 10 Ω -cm
Crystal Orientation	: $\langle 100 \rangle$
Wafer thickness	: 500 μ m

Table 3.3: Specifications of the SOI wafer used for fabricating the devices.

Doping	: P-type
Resistivity	: ~ 5 k Ω -cm
Crystal Orientation	: $\langle 100 \rangle$
Device Layer Thickness	: 5 μ m \pm 0.5 μ m
Box layer thickness	: 1 μ m
Handle wafer thickness	: ~ 500 μ m

As the waveguides were realized by deeper etching, these structures caused physical obstruction in the flow of PPR, resulting in incomplete coverage and non-uniformity. Hence the fabrication steps were chosen so that the coating of PPR is avoided after the realization of waveguides. Accordingly, gratings were realized first and then the waveguides. The process flow for this method is shown in Fig. 3.2. The major fabrication steps involved in each of the two mask processes were - cleaning, photoresist coating, photolithography, development and reactive ion etching.

Initially, the substrates were cleaned following the standard cleaning procedures with chemicals Trichloroethylene, Acetone, Isopropyl Alcohol, DI water, Piranha (APPENDIX C.3) and Hydrofluoric acid. This was done to remove the organic and inorganic contaminants present in the SOI surfaces. Then positive photoresist (PPR) - MicropositTM S1813 G2² was spin-coated onto the substrate.

²manufacturer: Rohm and Haas

Thus layer of thickness $\sim 2 \mu\text{m}$ was obtained on the SOI surfaces. The corresponding parameters used for the coating are given in Table. 3.4.

Table 3.4: Parameters used for the spin coating of PPR.

Speed	: 6000 rpm.
Acceleration	: 500 rpm/sec.
Time	: 60 sec.

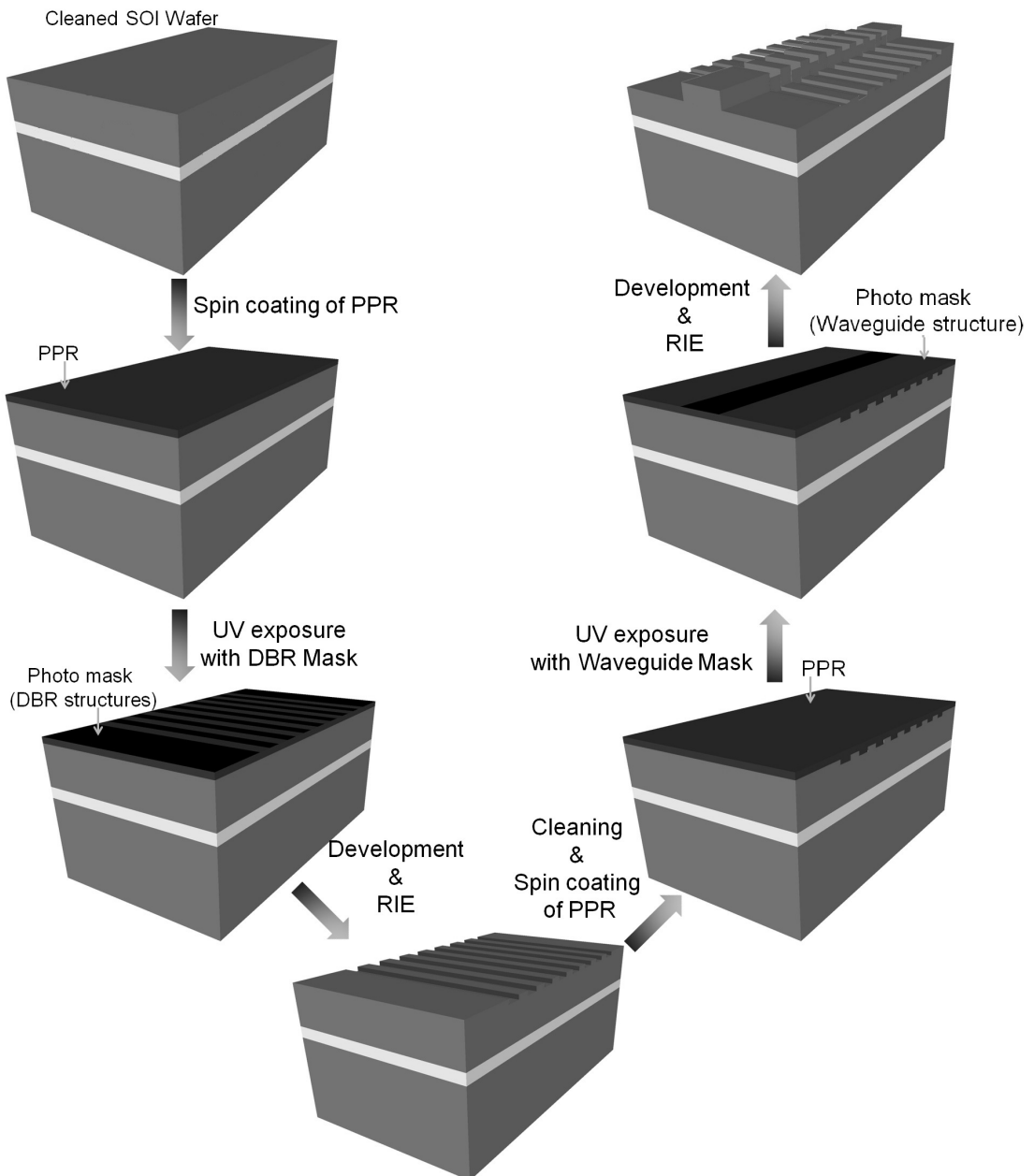


Figure 3.2: Fabrication process flow of DBR grating structure with large cross-section single-mode rib waveguides.

PPR was then hardened by pre-baking the sample in an 80°C oven for \sim

20 minutes. This was to avoid the sticking of PPR in the maskplate during contact photolithography. Using the MA6/BA6 mask aligner³, the samples were aligned with the photomask having the grating patterns and were exposed to UV ($\lambda=365$ nm (i-line); intensity ~ 3.7 mW/cm²). The samples were then subjected to post exposure bake in order to minimize the concentration gradient created during the exposure [39]. This process is important to avoid scalloping in the device edges and to improve the resolution of the resist patterns.

Development of the PPR was done using 0.1M NaOH solution (APPENDIX. C.1). The process steps were iterated by systematically varying the time for - prebake, exposure, post-exposure bake and development. Each time, the developed samples were visually inspected under microscope. The optimized timing which gave the best results are tabulated in Table. 3.5

Table 3.5: Optimized timings for prebake, exposure, post-exposure bake and development. The temperatures used and the typical lab ambient conditions measured during the process are also given.

Prebake	: 17 min.	inside 80°C oven
Exposure	: 13 s	at $\sim 25^\circ\text{C}$, $\sim 45\%$ humidity $\lambda=365$ nm (i-line) intensity ~ 3.7 mW/cm ²
Postexposure bake	: 5 min	inside 120°C oven
Development	: 50 to 55 sec	using 0.1M NaOH soln.

After development, the samples were post-baked at 120°C for ~ 40 min. to harden the PPR. Then the PPR patterns were transferred to the substrate by reactive ion etching (RIE). The etching chemistry was obtained from [40] and was optimized for our lab conditions. The corresponding values are given in Table. 3.6.

The O₂:SF₆:CHF₃ chemistry gave good verticality. However, the surface roughness was higher compared to SF₆:Ar chemistry (Recipe2). Fig. 3.3(a) and Fig. 3.3(b) are the scanning electron microscopic images of slab and gratings respectively after the RIE using Recipe1. The figures shows the verticality as well as the surface roughness resulted from the RIE process.

It was also observed that the top layer of PPR got removed during the etching.

³manufacturer: Suss MicroTec / Karl Suss

Table 3.6: Recipe used for RIE in the realization of gratings (Recipe1).

Gas flow rate	: O ₂ :SF ₆ :CHF ₃ ::15:25:10 sccm
Temperature	: 12°C
Pressure	: 50 mTorr
DC bias	: 335 V
RF power	: 150 W
Etch rate	: ~0.2 μm/min
Color of the plasma	: Bluish grey

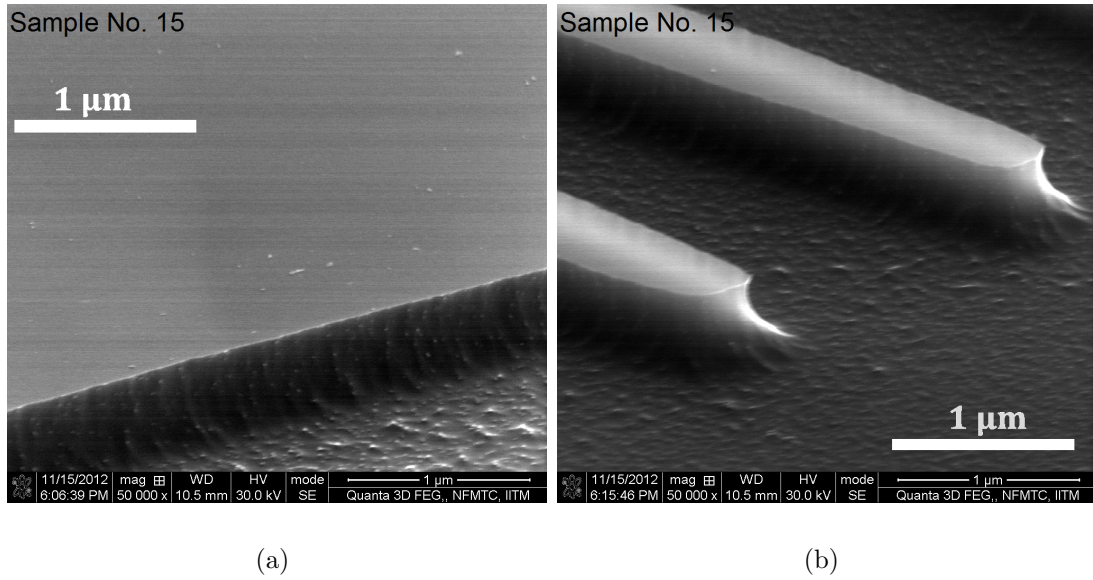
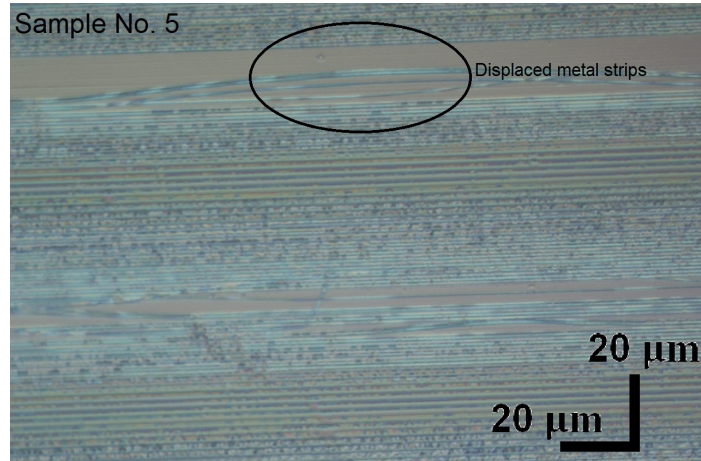


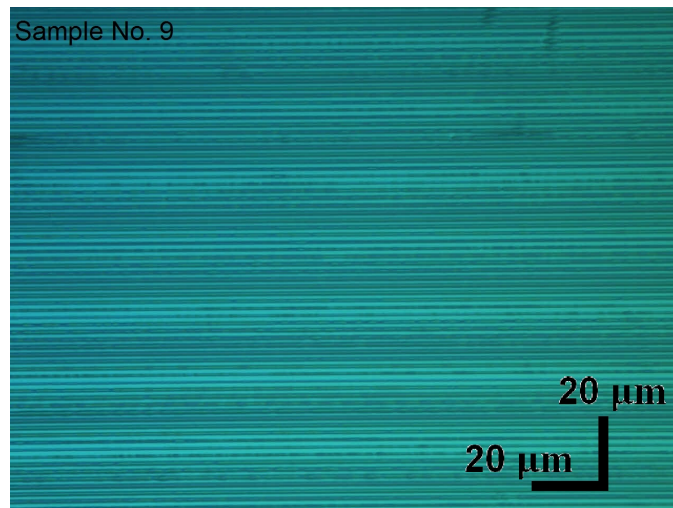
Figure 3.3: Scanning electron microscopic image of (a) slab and (b) gratings after RIE using Recipe1. The figures show the verticality of the sidewalls as well as the surface roughness introduced in the etched region.

Hence it was found that Recipe1 was not ideal for higher etch depths. But in case of the realization of gratings, as the etch depth required was only ~300 nm, PPR masks were continued in order to avoid the cost and delay involved in metallization. But, metal masks were also explored and were found unsuitable due to high aspect ratio of the grating teeth ($\sim 1 \mu\text{m} \times 550 \mu\text{m}$). The microscopic image in Fig. 3.4(a), shows the metal strips getting removed and displaced from the sample surface during development. Fig. 3.4(b) shows a the microscopic image of PPR mask on silicon substrate showing a good adhesion between them.

In the second step, the same procedures were carried out until RIE using the mask for waveguides. As we were using PPR masks and the etch depth required



(a)



(b)

Figure 3.4: Microscopic image of (a) metal mask and (b) PPR mask after development. Due to high aspect ratio of the metal strips ($\sim 1 \mu\text{m} \times 550 \mu\text{m}$) they got removed and displaced from the sample surface during development in sample 5.

in defining waveguides is $\sim 1.2 \mu\text{m}$, we switched to $\text{SF}_6:\text{Ar}$ chemistry in order to avoid the reaction with the PPR mask. The recipe used is given in Table. 3.7.

Fig. 3.5 shows the reconstructed image of the slab using confocal microscopy. The red plane in the top image shows the vertical observation plane and the bottom figure shows the etch profile in that plane. A small lateral misalignment between the first and second mask processes is evident from the kink in the vertical edges

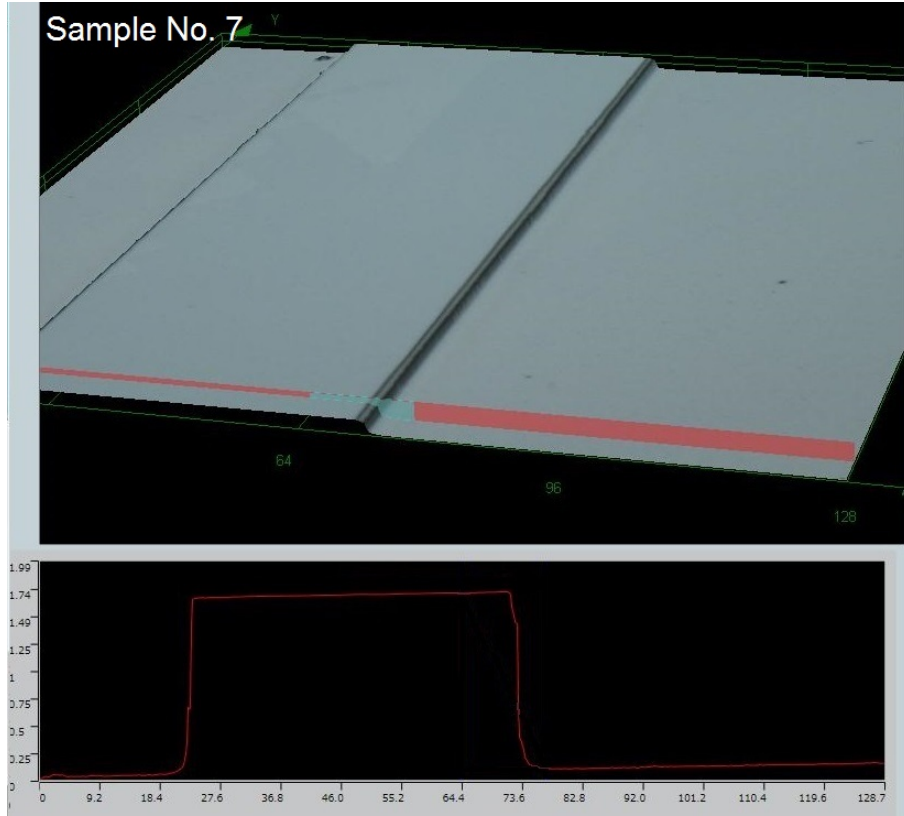


Figure 3.5: Reconstructed image of slab region using confocal microscopy. The red plane in the top image shows the vertical observation plane and the bottom figure shows the etch profile in that plane. A small lateral misalignment between the first and second mask processes is evident from the kink in the vertical edges of profile.

Table 3.7: Recipe used for RIE in the realization of waveguides (Recipe2).

Gas flow rate	: SF ₆ :Ar::20:20 sccm
Temperature	: 17°C
Pressure	: 200 mTorr
DC bias	: 35 V
RF power	: 150 W
Etch rate	: $\sim 0.35 \mu\text{m}/\text{min}$
Color of the plasma	: Pink

of profile. This is due to a slight shift of the second mask towards the left side. This lateral shift ($\sim 1 \mu\text{m}$) was well within the specifications of the aligner. As the gratings were designed to be wider than the waveguides, this misalignment did not effect the device performance.

For comparing the etch rates for Recipe1 and Recipe2, silicon samples were subjected to etching for different time duration using both the recipes. Fig. 3.6

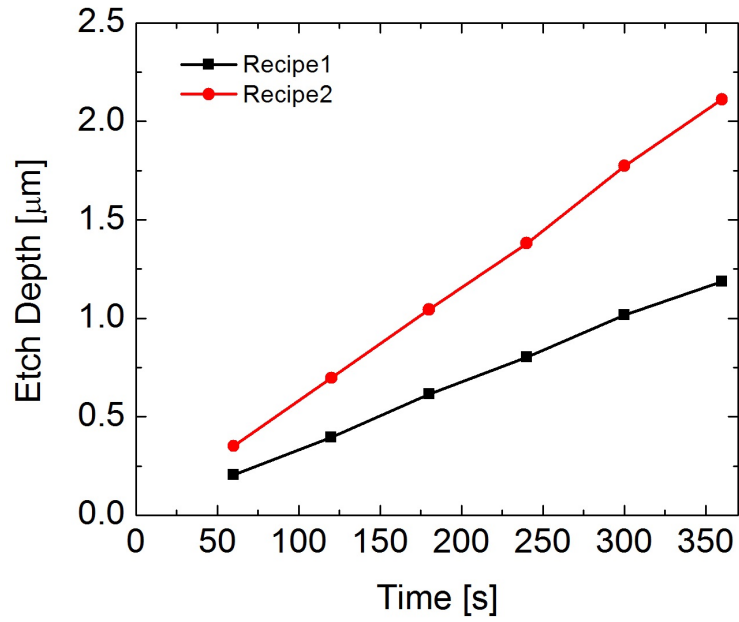


Figure 3.6: Comparison of the etch rates of Recipe1 and Recipe2. The etch rates were calibrated by 6 runs of RIE using each of the two recipes. The etch rates were found to be constant. The etch rates of Recipe1 and Recipe2 are $\sim 0.2 \mu\text{m}/\text{min.}$ and $\sim 0.35 \mu\text{m}/\text{min.}$, respectively.

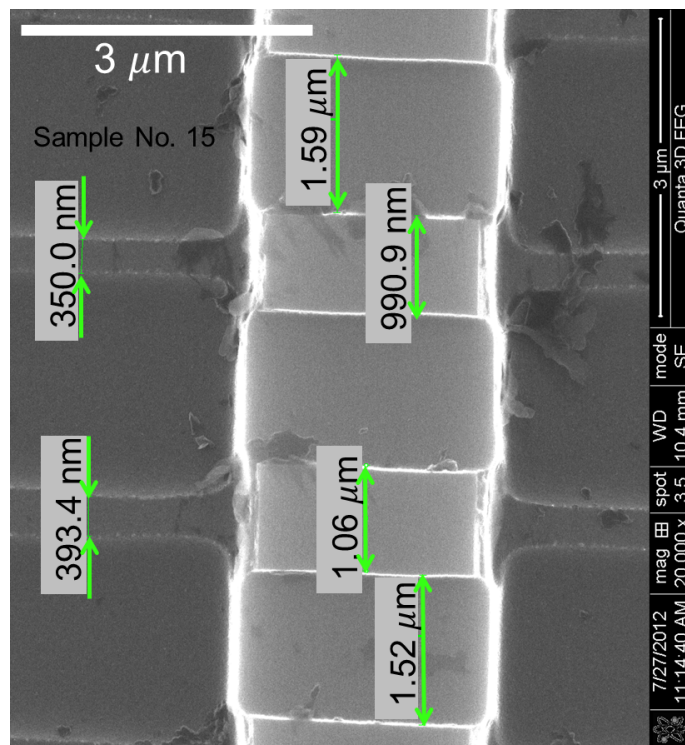


Figure 3.7: A typical scanning electron microscopic image zoomed in the grating regions for precise measurement of duty cycle.

compares the etch rates of the recipes. The etch rates were found to be constant-
 $\sim 0.2 \mu\text{m}/\text{min.}$ and $\sim 0.35 \mu\text{m}/\text{min.}$ for Recipe1 and Recipe2, respectively.

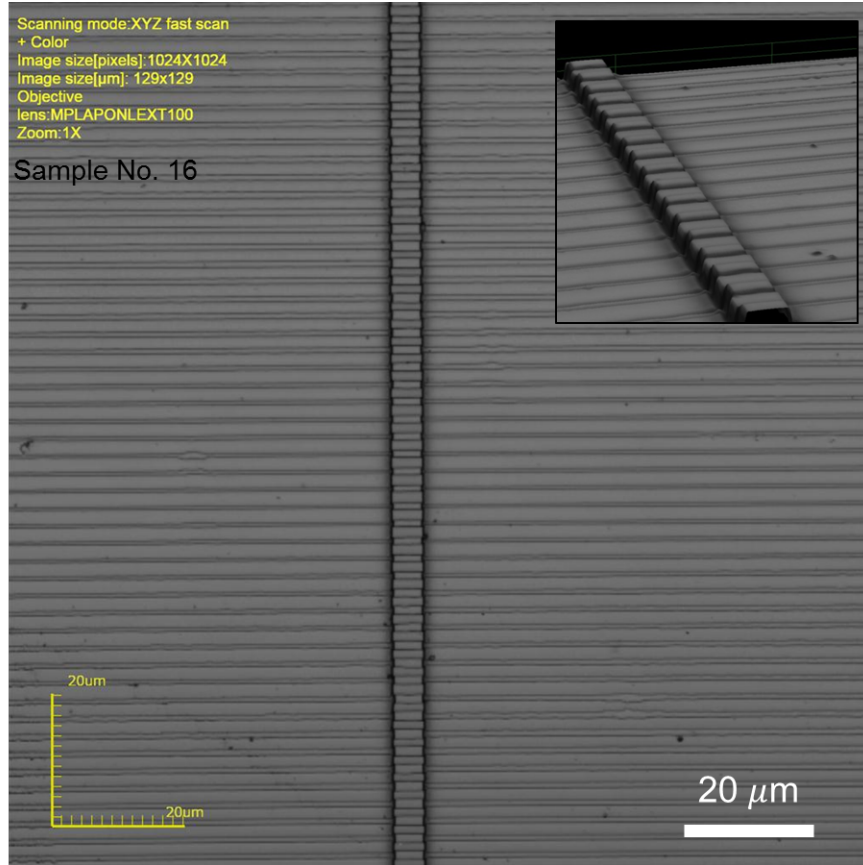


Figure 3.8: The confocal microscopic image showing the uniformity of the fabricated device. The figure in the inset is a reconstructed image from the depth measurements using the confocal microscope.

With the optimized parameters, the working devices were made in optical grade SOI wafers. The scanning electron microscopic image of the fabricated structure is shown in Fig. 3.7. Even though the period remained unchanged, the duty cycle of the gratings showed variations from the designed values due to over development (~ 100 nm). The duty cycle in the rib regions was found to be 0.4 which results in high reflectivity (see Fig. 2.17). The etching in the slab region during the realization of rib structure caused an additional maskless-etching of the gratings in the slab. The nonverticality of this etching process resulted in a lower duty cycle ($\sim 15\%$) for gratings in the slab region. Fig. 3.8 is a confocal microscopic image of the gratings at a lower magnification. Uniformity and verticality of the final structure can be seen in this image.

After the fabrication, the end facets of the devices were polished suitably to optical flatness. Typical microscopic images of the SOI edges after various grades

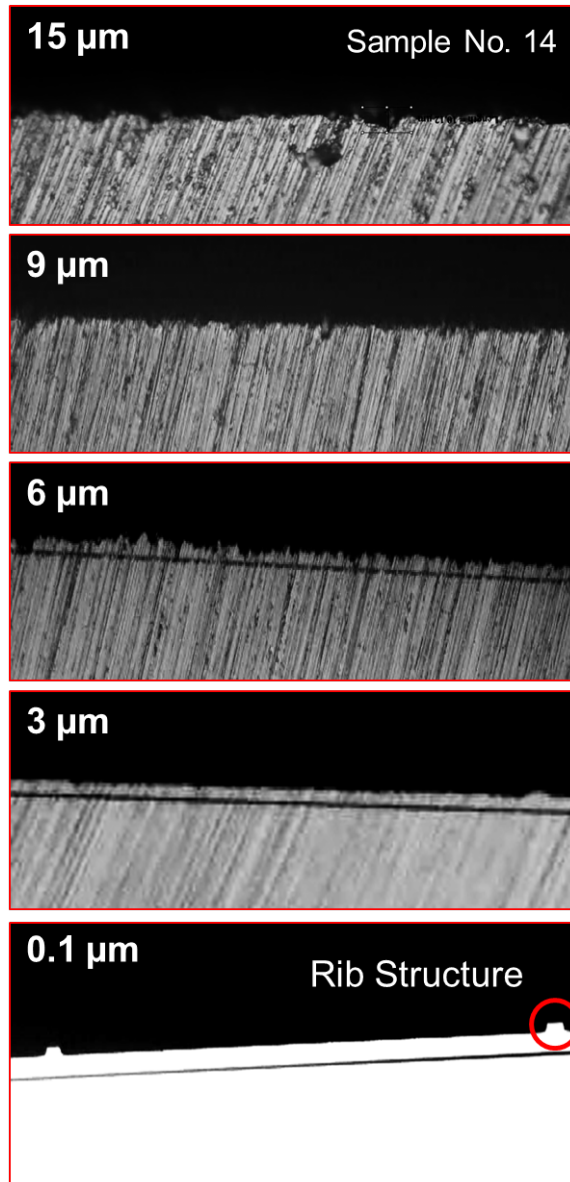


Figure 3.9: Typical microscopic images of the SOI edges after various grades of polishing. The roughness of the polishing film is gradually reduced from 30 μm to 100 nm. Correspondingly, the roughness in the edges also reduces. The rib and slab edges are clearly visible after the polishing with the 100 nm rough films.

of polishing are shown in Fig. 3.9. The polishing was done starting with a film of roughness 30 μm . It was continued until the cleaved edges become flat and perpendicular to the waveguides. Polishing was continued with films of decreasing roughness upto a 100 nm rough film. Correspondingly, the roughness in the end facet also got reduced. The rib and slab edges were clearly visible after polishing with 100 nm rough films.

3.3 List of Fabricated Devices

Si samples were used for optimizing the fabrication parameters. As there is no vertical confinement for waveguiding in silicon samples, they were used only for studying the surface profiles. SOI samples were used for both structural and optical characterizations. The list of some of the devices on Si and SOI substrate are enlisted in Table. 3.8 and Table. 3.9, respectively.

Table 3.8: List of some of the important silicon samples. These samples were used for optimizing the fabrication processes as well as for studying the surface profiles.

Sample No.	SWG etch depth	Grating etch depth	Remarks
01	1.5 μm	-	Overdeveloped. The waveguide widths were reduced.
02	1.2 μm	-	White patches even after agitation, heating and chemical treatment.
03	1.2 μm		Good straight waveguides of length 1.5 cm
04	1.2 μm		Good straight waveguides Total length 2 cm
05	-	-	Metal mask was peeling off. Not proceeded for etching
06	1.5 μm	200 nm	Overdeveloped (lower duty cycle)
07	1.4 μm	340 nm	Reasonably good. Grating lengths 3 mm, 5 mm, 7 mm. Total length 13 mm.
08	1.2 μm	310 nm	Nonuniform development. Total length 15 mm.
09	1.2 μm	270 nm	Good. Grating length 1 mm, 3 mm, 5 mm. Total length 11 mm.
10	1.2 μm	270 nm	Good. Grating length 2 mm, 4 mm 6 mm. Total length 9 mm.

Table 3.9: List of some of the important SOI samples. These samples were used for both optical characterizations as well as for studying the surface profiles.

Sample No.	SWG etch depth	Grating etch depth	Remark
11	1.5 μm	-	Dust and white precipitates
12	1.2 μm	-	Good. Total Length 8 mm.
13	1.5 μm	250 nm	No guiding. Rough and lossy.
14	1.5 μm	200 nm	Very low reflectivity.
15	1.2 μm	250 nm	Good. Grating lengths 0.6 mm, 2.6 mm. Total length 8 mm. 4 devices.
16	1.2 μm	260 nm	Good. Grating length 5.2 mm. Total length 9.3 mm. 15 devices.

3.4 Experimental Results and Discussions

After polishing, the devices were characterized, measuring their loss, mode profile and spectral response. Each of them are presented in following subsections.

3.4.1 Waveguide Loss and Mode Profile

The devices were characterized using the setup shown in Fig. 3.10. The light from the laser was first directed through a polarization controller to a fiber mount from which the light diverges. As the input fiber used in this experiment was not polarization-maintaining, the fiber path from the laser source to the fiber mount was clamped to the table to prevent the alteration of polarization state due to unintentional fiber deformations. A lens assembly consisting of an input collimator and a focusing lens were used to couple the laser into the input side of the device under test (DUT). A Glan-Thompson polarizer was used after the collimator in order to fix the polarization axis. The polarization controller was adjusted so as to maximize the input power in the selected polarization. From the output of the DUT, the light was again focused into the fiber leading to OSA using a similar collimator-focusing lens assembly. Further, an iris was used to

spatially filter the collimated light at the output. This prevented substrate-guided radiation and stray light from entering into the fiber.

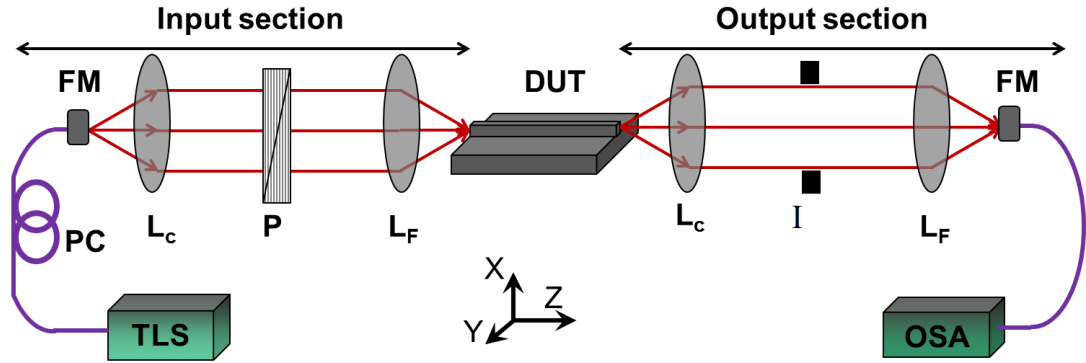


Figure 3.10: Schematic of the setup for measuring the transmission characteristics of the fabricated devices: TLS-Tunable Laser Source, PC-Polarization Controller, FM-Fiber Mount, L_C -Collimating Lens, P-Polarizer, L_F -Focusing Lens, DUT-Device Under Test, I-Iris, OSA-Optical Spectrum Analyser.

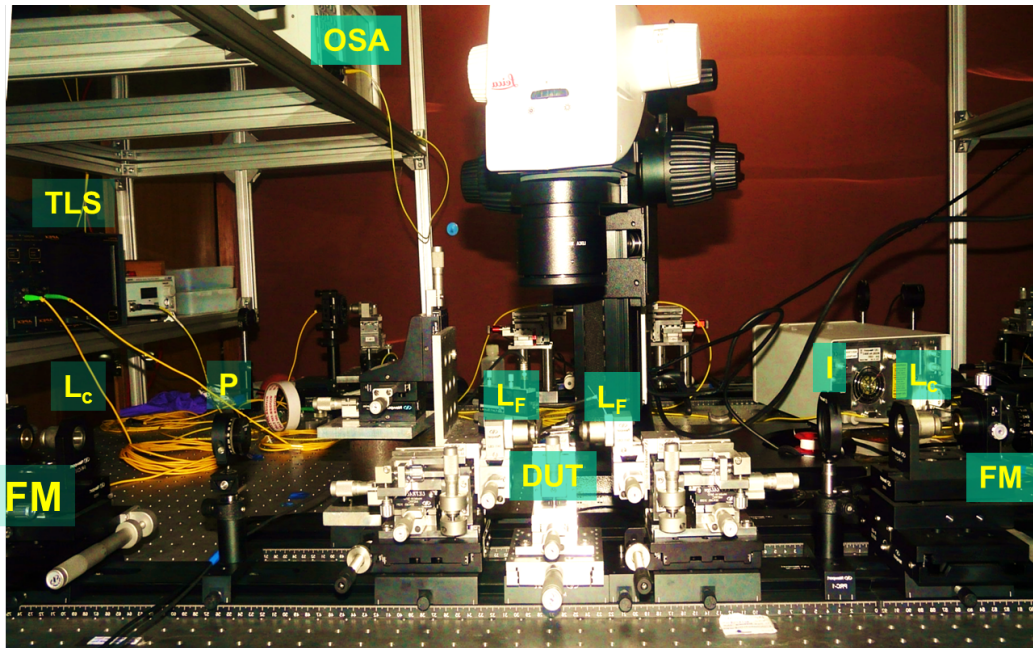


Figure 3.11: Photograph of the setup for measuring the transmission characteristics of the fabricated devices: TLS-Tunable Laser Source, FM-Fiber Mount, L_C -Collimating Lens, P-Polarizer, L_F -Focusing Lens, DUT-Device Under Test, I-Iris, OSA-Optical Spectrum Analyser.

Initially, the transmission characteristics of the waveguides were taken and the loss was estimated using Fabry-Perot loss measurement technique [16]. In this technique we consider the waveguides as lossy Fabry-Perot cavities with Si-

air interface at the two end faces acting as reflectors. Assuming vertical and smooth endfaces, the internal reflectivity of the waveguide end facets, R_{FP} can be calculated from the index contrast using the formula

$$R_{FP} = \left| \frac{n_{eff} - 1}{n_{eff} + 1} \right|^2 \quad (3.1)$$

where n_{eff} is the effective index of the waveguides. Thus for the waveguides we have fabricated, R_{FP} was estimated to be $\sim 30\%$. Typical to Fabry-Perot cavities, constructive and destructive interference occur for wavelengths $\lambda_c = \frac{2Ln_{eff}}{m}$ and $\lambda_d = \frac{4Ln_{eff}}{2m+1}$ respectively where L is the length of the waveguide. Hence the transmission characteristics (around the wavelength λ) will have alternate maxima and minima with a free spectral range, FSR given by

$$FSR = \frac{\lambda^2}{2n_{eff}L} \quad (3.2)$$

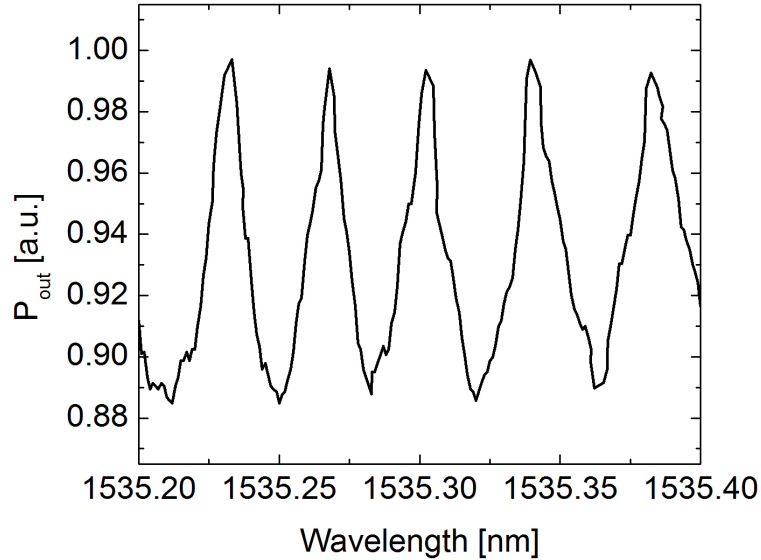


Figure 3.12: Normalized transmission spectrum for TE polarization through a rib waveguide ($H=5 \mu m$, $h=3.8 \mu m$ and $W=3.5 \mu m$). The measured FSR of 40 pm and the estimated value is 36 pm for a waveguide length of ~ 9.3 mm.

Fig. 3.12 shows the transmission characteristics of one of the waveguide considered with peak output power normalized to 1 mW. The waveguide had a length

of ~ 9.3 mm. Value of FSR estimated from eqn. 3.2 was 36 pm and was found to be close to the experimental value of 40 pm. The loss of the waveguides, α can be measured using the formula

$$\alpha = \frac{1}{L} \ln \left(\frac{\zeta}{R_{FP}} \right) \quad (3.3)$$

where ζ is the contrast of the Fabry-Perot response, defined as

$$\zeta = \frac{\sqrt{I_{max}} - \sqrt{I_{min}}}{\sqrt{I_{max}} + \sqrt{I_{min}}} \quad (3.4)$$

I_{max} and I_{min} are the maximum and minimum output intensities from the waveguide. For the best waveguides, the propagation loss, α was estimated to be ~ 0.24 dB/mm.

One of the advantages of the Fabry-Perot loss measurement as evident from eqn. 3.3 is that the loss measurement is independent of the coupling efficiency and other external losses. However, the loss estimate is highly dependent on the reflectivity of the the end facets, R_{FP} . Hence, misaligned, rough or non vertical end facets can attribute to errors in this method of loss estimation.

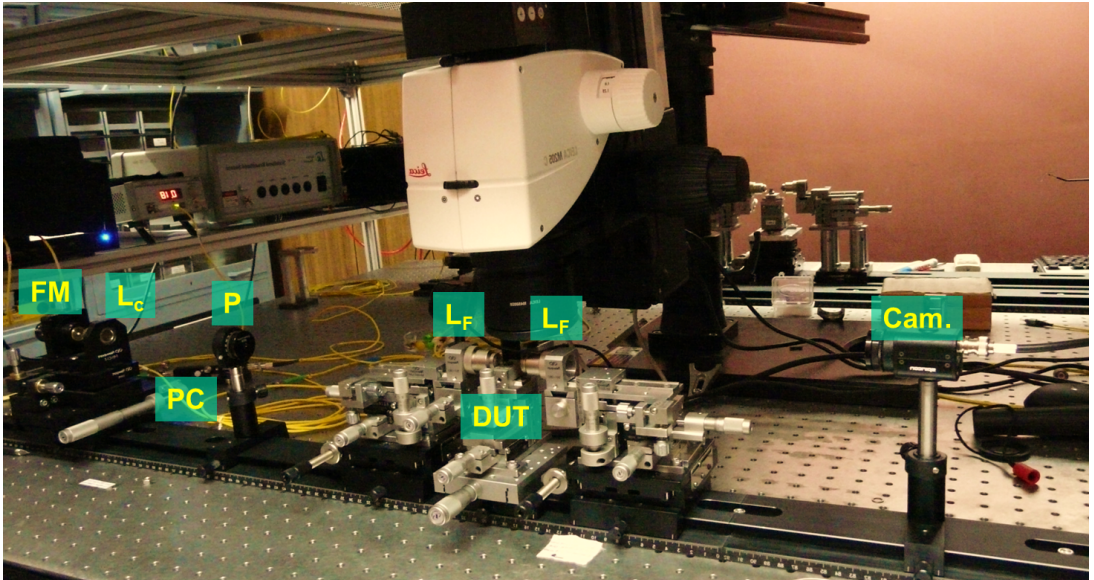


Figure 3.13: Photograph of the setup for measuring the mode profile of the fabricated devices: PC-Polarization Controller, FM-Fiber Mount, L_C -Collimating Lens, P-Polarizer, L_F -Focusing Lens, DUT-Device Under Test, Cam-Camera

The mode profiles of the fabricated structures were obtained from the profile of the output intensity distribution. Similar to the setup for measuring the transmission characteristics, the mode profile measurement setup shown in Fig. 3.13 consisted of a tunable laser source, lens assembly, polarizer and polarization controller. But at the output section, the light emerging out of the DUT was focused to a Charge Coupled Device (CCD) camera. The CCD camera was interfaced with a computer through a camera frame-grabber card.

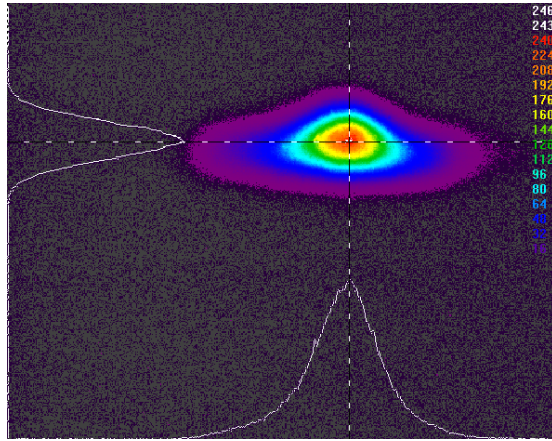


Figure 3.14: Observed mode profile for TE input polarization at $\lambda \sim 1530$ nm for waveguide width, $W = 3.5 \mu\text{m}$. This well confined mode confirms the proper guiding of light through the rib structure. Comparing this profile with the mode profile obtained from a standard single-mode fiber, the size of the mode was estimated to be $\sim 8\mu\text{m} \times 15\mu\text{m}$ (tolerance in measurement $2 \mu\text{m}$).

The input and output focusing lenses were both mounted on a 3-axis stage (x, y and z translation axes). The chip containing the DUT was also mounted on a translation stage. The alignment stages were adjusted to maximize the power coupled into and out of the device. This was made sure by measuring the power just in front of the camera using a power meter. Then the input power was reduced so that the output power is < 0.1 mW. This was to reduce the intensity of the output profile so as to keep the CCD array out of saturation. Later the power meter was removed and the mode profile was focused into the CCD sensor array of the camera. The mode profiles were taken using a camera frame-grabber and a computer. A typical mode profiles for TE input polarization at $\lambda \sim 1530$ nm for waveguide width, $W = 3.5 \mu\text{m}$ is shown in Fig. 3.14. Well confined modes at the output section, confirms the proper guiding of light through the rib structure.

3.4.2 Spectral Response

The optical characterization of the DBR structures were carried out in our free space characterization setup as shown in Fig. 3.10. The input and output focusing lenses were both mounted on a 3-axis stage (x, y and z translation axes). The chip containing the DBRs were also mounted on a translational stage. The alignment stages were adjusted to maximize the power coupled into the device as well the power coupled into the output fiber. The alignment was done using a 20 mW IR source where as the actual characterization was done using the inbuilt tunable laser (tunability 0.8 pm) from the OSA.

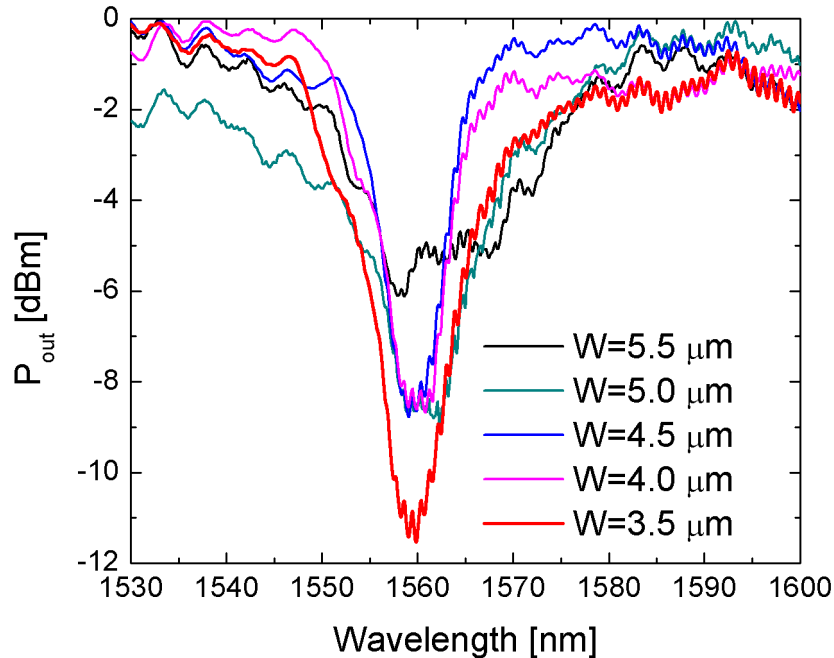


Figure 3.15: Observed grating responses from the fabricated samples for TE polarization. The parameters of the fabricated device are: $\Lambda = 2.6 \mu\text{m}$, $e = 260 \text{ nm}$, $L = 5.2 \text{ mm}$, $H = 5 \mu\text{m}$, $h = 3.8 \mu\text{m}$. The width, W is varied from $5.5 \mu\text{m}$ to $3.5 \mu\text{m}$. The spectrum is normalized with the transmission spectrum of waveguides and for a peak output power of 1 mW.

Fig. 3.15 shows the response from a set of 5 gratings for TE Polarization. The response showed a peak reflectivity, $R > 90\%$ and full width at half maxima $\sim 4 \text{ nm}$ for a waveguide width of $3.5 \mu\text{m}$.

3.4.3 Discussions

Waveguiding in the devices were assured by observing the output mode profile. The propagation loss of waveguides were found to be ~ 0.24 dB/mm. Comparing the transmitted power from the DBRs and waveguides, the propagation loss in DBRs were estimated to be 1.5 dB/mm.

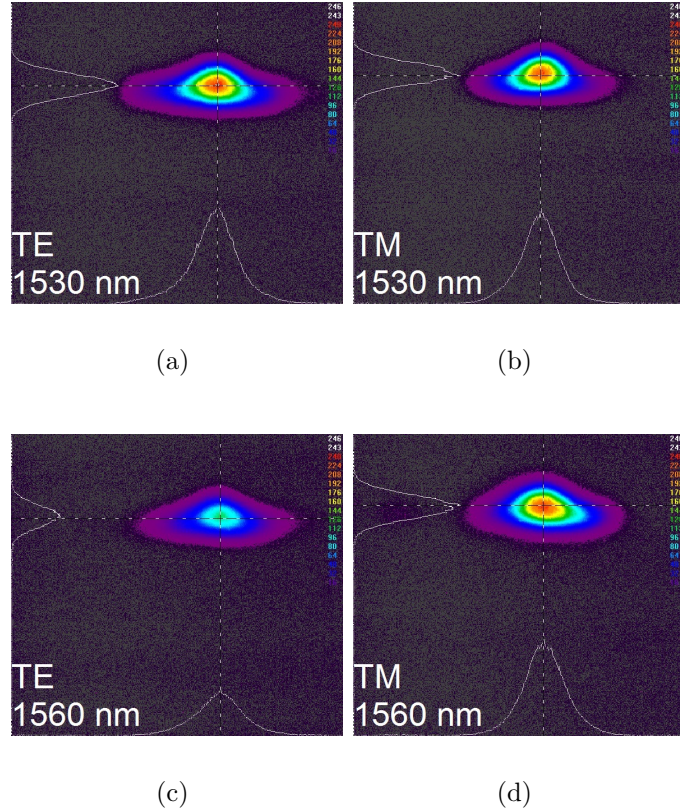


Figure 3.16: Observed mode profiles for TE and TM input polarizations for phase-matched ($\lambda = 1560$ nm) and phasemismatched ($\lambda = 1530$ nm) wavelengths for waveguide width, $W = 3.5 \mu\text{m}$. The reduction in the transmitted power for TE polarization for phase-matched wavelength is observed in the reduced intensity of the corresponding mode.

The mode profiles of the DBR structures for the same input power (after polarizer) for TE and TM input polarizations for phase-matched ($\lambda = 1560$ nm) and phasemismatched ($\lambda = 1530$ nm) wavelengths are given in Fig. 3.16. It is evident from the mode profiles that even after the introduction of DBR in the waveguides, the modes were found to maintain transverse profile. It was also observed that the output intensity of TE polarization was reduced significantly in the phase-matched wavelength whereas the output intensity of TM polarization

was almost wavelength independent.

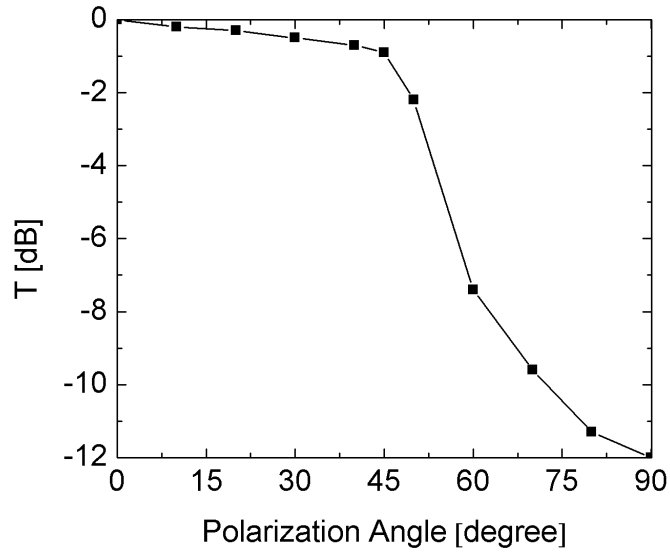


Figure 3.17: Normalized transmission at phasematched wavelength as a function of polarization angle. This figure shows the polarization dependence of the device.

Eventhough the devices were designed for TE polarization, the polarization dependence was studied by measuring the transmission at the phase matched wavelength as the input polarization is systematically changed from TE (90°) to TM (0°). The corresponding result is shown in Fig. 3.17. It shows that only TE polarization had a -12 dB reduction in transmitted power at the phasematched wavelength. Further, no transmission dips were found in the range 1530 nm to 1600 nm for TM polarization. This variation in the response of TE and TM polarization is expected to be due to birefringence in Bragg structures as suggested by Richter et.al.[41].

Another observation was the shift in the reflection peak from the understanding of coupled mode theory described earlier. The period required for the phase-matching at ~ 1560 nm was $\sim 2.5 \mu\text{m}$ where as we obtained the reflection peak at ~ 1560 nm for a period of $2.6 \mu\text{m}$. Similar observations were reported by Giuntoni et.al. [42] after an extensive numerical survey on Bragg reflectors. The analytic phase matching condition can only serve as a guide line for choosing the grating period and as a function of grating depth and duty cycle, the reflectivity shifts towards shorter wavelengths [42]. This is due to the reduction in average fundamental modal index in a grating structure.

The work presented in this chapter can be summarized as follows. The devices were fabricated by lithography using i-line UV and subsequent RIE. A two step fabrication process was used for this purpose. Exposure and baking parameters were optimized for realization of small openings. RIE processes were calibrated for two different chemistry. The surface profiles of the final structures were studied while optimizing the parameters.

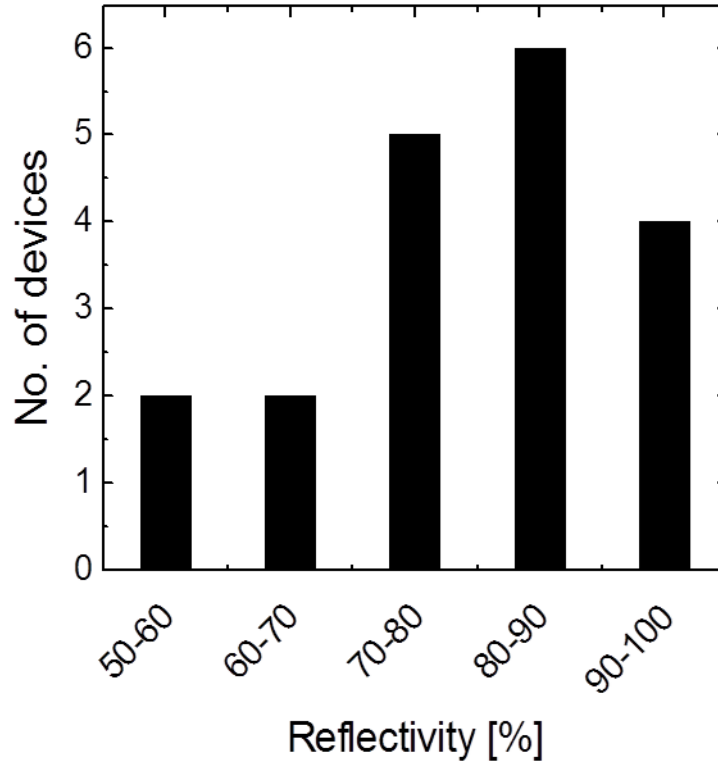


Figure 3.18: Histogram of peak reflectivity obtained from the final devices. In total 19 devices were found to be having more than 50% reflectivity.

The fabricated devices were polished and were characterized in our free space coupling setup. The initial devices were found to be very inefficient. With repetition, the device performance got improved along with the improvement in fabrication skill. The reproducibility of these devices were checked by fabricating multiple devices and measuring their reflectivity. The reflectivities obtained from the fabricated samples is given as a histogram in Fig. 3.18. In total 19 devices were found to be having more than 50% reflectivity. The dimensions of the final fabricated devices are tabulated in Table. 3.10.

The final characterization results showed a peak-reflectivity $R_{\max} > 90\%$,

Table 3.10: Final parameters of the integrated optical DBR structure on large cross-section rib waveguides after fabrication.

Parameter	Symbol	Value
Rib height	H	5.0 μm
Slab height	h	3.8 μm
Waveguide width	W	3.5 μm to 5.5 μm
Grating Period	Λ	2.6 μm
Duty Cycle	p	0.4
Grating Length	L	2.6 mm, 5.2 mm

FWHM = 3.3 nm (estimated from transmission spectrum). The propagation loss of waveguides and DBRs were found to be ~ 0.24 dB/mm and ~ 1.5 dB/mm, respectively.

CHAPTER 4

CONCLUSIONS

4.1 Summary

Design, fabrication and characterization of integrated optical DBR structures have been carried out under the scope of my MS research work.

First, the design of large cross section single mode rib waveguide was carried out. Then the design of grating structures using coupled mode theory was done. Considering the approximations of coupled mode theory and fabrication limitations in the lab, suitable dimensions for waveguide and gratings were decided. Also the influence of various grating and waveguide parameters on the grating response were studied and the critical parameters were identified.

The mask design and mask fabrication were carried out. Lithography using i-line UV was carried out for the realization of the devices. The method of post exposure baking was explored and was found to be useful in the realization of small openings. RIE processes were calibrated using $O_2:SF_6:CHF_3$ chemistry for shallow etched, vertical grating structures. It was found to be not suitable for deeper etching when PPR mask was used. A milder, $SF_6:Ar$ chemistry was used for the realization of rib structures. The verticality of the etching as well as the quality of the fabrication procedures were observed using confocal micrography, scanning electron micrography and surface profiling.

The fabricated devices were polished to an optical flatness and were characterized in our free space coupling setup. The final characterization results showed a peak-reflectivity $R_{max} > 90\%$, FWHM = 3.3 nm (estimated from transmission spectrum). The propagation loss of waveguides and DBRs were found to be ~ 0.24 dB/mm and ~ 1.5 dB/mm respectively.

These higher order DBRs can provide a cost effective method for the fabrication of discrete DBR-based optical devices. Also this method can provide a simpler alternative for conventional grating structures in other integrated optoelectronic devices. Unlike the first order DBRs the interaction length is longer in these structures. Hence these structures are better suited for sensing applications.

4.2 Outlook

DBRs and gratings are very versatile devices and there are immense possibilities for them which can be further investigated. Some of the possible improvements and suggestions are listed below

1) Higher reflectivity and narrower grating response can be achieved by further increasing the grating length.

2) The waveguide loss has been increased because of the surface roughness during the RIE process for grating fabrication. It can be reduced by a subsequent blanket RIE.

3) In this work, the reflection spectrum was not measured directly because the coupling techniques used in this method produced unintentional back reflections. A modified device design which can measure the transmission and reflection spectrum simultaneously is given in Fig. 4.1. Free space coupling can be used at the input port (P_{in}) and butt coupling using ribbon fibers can be done at the output ports (P_2 and P_3). The transmission and reflection spectrum of the DBR can be obtained at P_2 and P_3 respectively. This can also be used as an add-drop multiplexer at the wavelength λ_{DBR} .

4) A simulation tool has to be developed in order to analyse the structure with a fewer pre-assumptions and approximations. It could be used for studying the polarization dependent response and identifying the exact position of grating peak and bandwidth. From the carried out literature survey, it was identified that finite difference time domain method and bi-directional eigen mode expansion method are widely used in the analysis of grating structure.

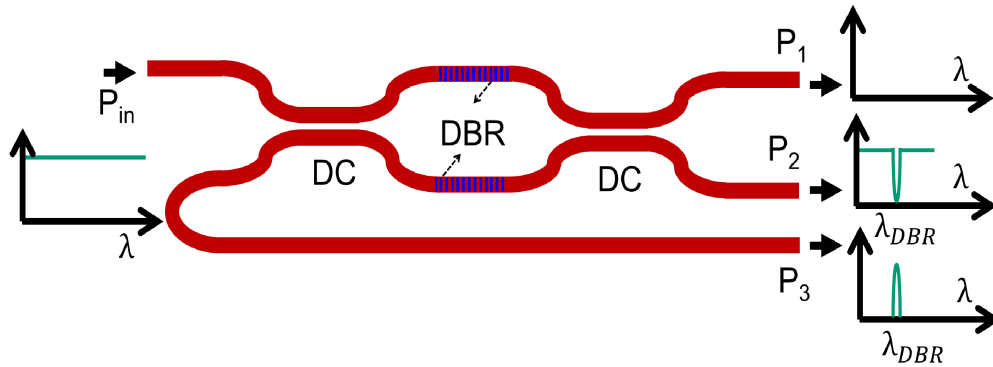


Figure 4.1: Schematic of the modified design. DC: Directional Coupler, DBR: Distributed Bragg Reflectors, P_{in} : Input Port, $P_{1,2,3}$: Output Ports.

5) The possibilities of lower order DBRs have to be explored with the availability of new fabrication facilities. Eventhough first order DBRs are fabricated with different (deep UV or e-beam) lithography processes; theoretical analysis, RIE parameters and characterization procedureds can be similar to those mentioned in this work. Also, other devices based on grating structures such as Fabry-Perot etalons, dispersion compensators and add-drop multiplexers can also be realized using gratings and DBRs.

APPENDIX A

DERIVATIONS

A.1 Calculation of Coupling Coefficient

In this subsection, an outline of the derivation of coupled equations due to dielectric perturbation in a single mode waveguide is given. Emphasis is given to the calculation of coupling coefficient in a grating realized by periodic surface corrugation of a rib waveguide. The dependence of the coupling coefficient and the shape of the grating is derived in terms of the Fourier coefficients.

Maxwell's equations are first order coupled differential equations in electric and magnetic fields. They can be uncoupled into two separate second order equations - wave equations - for electric and magnetic fields [43]. With a proper choice of axes, a waveguide with a uniform cross section can be defined in terms of a two dimensional dielectric function. The solution of wave equations in such a waveguide can be expressed as a linear combination of discrete modes. These modes are the (orthogonal) eigen solutions of Maxwell's equation in that waveguide. In a single mode waveguide, only a pair of counter propagating modes (with phase constants β_1 and $-\beta_1$) with the same mode profile is possible. Hence the total electric field in such waveguide reduces to a linear combination of two counter propagating mode. The coupled equations relating their amplitudes A_1 and A_2 are given by:

$$\begin{aligned}\frac{dA_1(z)}{dz} &= -j\kappa A_2(z)e^{j\Delta\beta z} \\ \frac{dA_2(z)}{dz} &= j\kappa^* A_1(z)e^{-j\Delta\beta z}\end{aligned}\tag{A.1}$$

Here $\Delta\beta$ is the phase mismatch between the propagation constants of the two modes and κ_m is the coupling coefficient between these two modes. In an unperturbed waveguide, as a consequence of the orthogonality of the counter propagat-

ing modes, κ_m is zero. However, the introduction of any non-uniformity in the waveguides can be incorporated by an additional dielectric perturbation function $\Delta\epsilon$. In case of small perturbation, we assume that the mode profiles remain intact as in the unperturbed waveguide. Then, the coupling coefficient κ is given by

$$\kappa = \frac{\omega}{4} \iint E^* \Delta\epsilon E \, dx \, dy \quad (\text{A.2})$$

where E is the electric field distribution of the single mode. Even now, with a non-zero coupling coefficient, there will not be any effective power transfer between the modes because of large non-zero value of $\Delta\beta$. In the specific case of gratings, the analysis is carried out by expanding the perturbation in terms of Fourier series as given by

$$\Delta\epsilon = \sum_m \mathcal{F}_m[\Delta\epsilon] e^{-jm\frac{2\pi}{\Lambda}z} \quad (\text{A.3})$$

Here, we assumed that the perturbation is periodic in the z-direction with a fundamental period Λ . $\mathcal{F}_m[\Delta\epsilon]$ is the m^{th} coefficient in the Fourier series expansion of the dielectric perturbation $\Delta\epsilon$. Thus the coupling coefficient due to the m^{th} Fourier coefficient of the dielectric perturbation is given by

$$\kappa_m = C_m I \quad (\text{A.4})$$

Here, I is the overlap integral between the normalized modes in the grating region. Its expression as well as the procedure for its calculation are given in sec. 2.2.2. C_m is given by

$$C_m = \frac{\omega}{4} \mathcal{F}_m[\Delta\epsilon] \quad (\text{A.5})$$

In case of the gratings realized by periodic etching of waveguides with air cladding, C_m can be simplified as

$$C_m = \frac{\omega}{4} \epsilon_0 (n_{eff}^2 - 1) \mathcal{F}_m[s(z)] \quad (\text{A.6})$$

where n_{eff} is the effective index of the waveguiding structure and $s(z)$ is the

function representing the shape of the grating. The expressions for $s(z)$ for some of the well known structures and the amplitudes of their m^{th} Fourier coefficient are given below:

Rectangular Grating (duty cycle = p)

$$s(z) = \begin{cases} 0, & 0 < z < p \\ 1, & p \leq z < \Lambda \end{cases}; \quad |\mathcal{F}_m[s(z)]| = \frac{\sin(mp\pi)}{m\pi}$$

Square Grating (duty cycle = 0.5)

$$s(z) = \begin{cases} 0, & 0 < z < \frac{\Lambda}{2} \\ 1, & \frac{\Lambda}{2} \leq z < \Lambda \end{cases}; \quad |\mathcal{F}_m[s(z)]| = \frac{\sin(m\pi/2)}{m\pi}$$

Symmetric Triangular Grating

$$s(z) = \begin{cases} z, & 0 < z < \frac{\Lambda}{2} \\ \frac{\Lambda}{2} - z, & \frac{\Lambda}{2} \leq z < \Lambda \end{cases}; \quad |\mathcal{F}_m[s(z)]| = \frac{\sin^2(m\pi/2)}{(m\pi)^2}$$

Gratings with Arbitrary Shape

The Fourier coefficient of any arbitrary shape can be found out numerically by using Discrete Fourier Transform (DFT). For this procedure, the shape has to be sampled at discrete points. For accurate results, the sampling must be done at sufficiently large rates. Then standard Fast Fourier Transform (FFT) algorithms can be used to obtain the Fourier coefficients. APPENDIX B.3 presents an example MATLAB code for finding the DFT of a trapezoidal structure.

APPENDIX B

PROGRAMMING

B.1 RSOF T Code Representing a Rectangular Element

Fig. B.1 shows the graphical representation of a typical mask element (segment 5069) in the RSOF T™ CAD Tool. Equivalently this is also represented by a segment of code using the format followed by RSOF T.

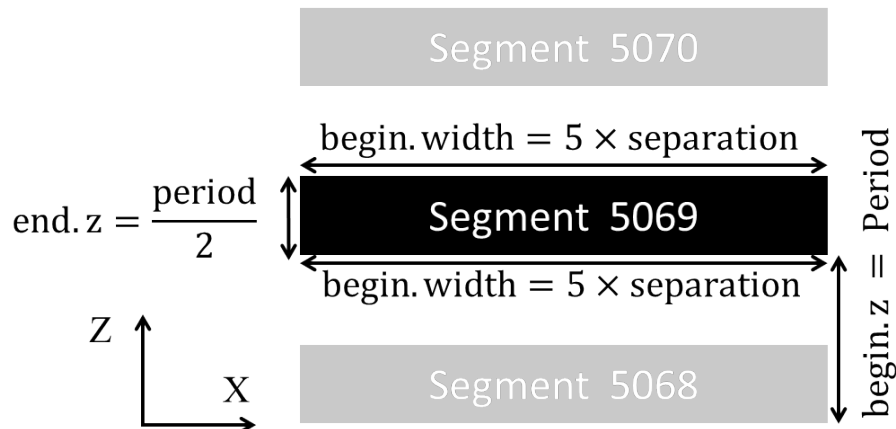


Figure B.1: Representation of a typical mask element (segment 5069) in the RSOF T CAD tool. The beginning of the element is defined relative to the beginning position of the previous element (segment 5068) where as the width ($5 \times \text{separation}$) and the thickness ($\text{period}/2$) of the element are defined in terms of absolute lengths. *period* and *separation* are variables defined at the beginning of the code

The attributes of this segment are:

- Segment 5069 has the same x co-ordinates as that of segment 5068
- It is one *period* away from segment 5068 in z direction. Numerical value of the variable *period* is defined at the beginning of the code and is changed as per the requirement ($2.3 \mu\text{m}$ to $2.6 \mu\text{m}$).
- It has a uniform width of $5 \times \text{separation}$. Numerical value of the variable *separation* is defined as $110 \mu\text{m}$ at the beginning of the code.

- Its span in the z-direction is *period*/2 which makes the duty cycle 50%.

RSOFT code

```
segment 5069
  begin.x = 0 rel begin segment 5068
  begin.z = period rel begin segment 5068
  begin.width = 5*separation
  end.x = 0 rel begin segment 5069
  end.y = 0 rel begin segment 5069
  end.z = period/2 rel begin segment 5069
  end.width = 5*separation
end segment
```

B.2 C Code for Generating the RSOFT Elements

Sample C code

```
%%%%%%%%%%%%%%%%%%%%%%%%%%%%%%%%%%%%%%%%%%%%%%%%%%%%%%%%%%%%%%%%%%%%%%%%
% This c code generate the RSOFT code for 5000 grating elements %
% begining from 5069th element. The corresponding RSOFT code %
% will be in the file 'harish.txt' in the same folder. %
% Include files required : stdio.h %
%%%%%%%%%%%%%%%%%%%%%%%%%%%%%%%%%%%%%%%%%%%%%%%%%%%%%%%%%%%%%%%%%%%%%%%%

#include <stdio.h>

void main()
{
  int i;
  FILE *fff;
  int starting = 5069; %count of the first element
  int nu_of_gratings = 5000; %total number of elements
```

```

                                %to be generated
int relative_to = 5068; %intial element to be related upon
int ending;
ending=starting+nu_of_gratings;
    fff = fopen("harish.txt","w");

fprintf(fff,"segment %d\n",starting);
fprintf(fff,"\tbegin.x = 4*seperation
            rel begin segment %d\n",relative_to);
fprintf(fff,"\tbegin.z = Length/2+200-glenght1/2
            rel begin segment %d\n",relative_to);
fprintf(fff,"\tbegin.width = 5*seperation\n");
fprintf(fff,"\tend.x = 0 rel begin segment %d\n",starting);
fprintf(fff,"\tend.y = 0 rel begin segment %d\n",starting);
fprintf(fff,"\tend.z = period1/2 rel begin segment %d\n"
            ,starting);
fprintf(fff,"\tend.width = 5*seperation\n");
fprintf(fff,"end segment\n");
for (i=starting+1;i<ending;i++)
{
fprintf(fff,"\nsegment %d\n",i);
fprintf(fff,"\tbegin.x = 0 rel begin segment %d\n",i-1);
fprintf(fff,"\tbegin.z = period2 rel begin segment %d\n",i-1);
fprintf(fff,"\tbegin.width = 5*seperation\n");
fprintf(fff,"\tend.x = 0 rel begin segment %d\n",i);
fprintf(fff,"\tend.y = 0 rel begin segment %d\n",i);
fprintf(fff,"\tend.z = period2/2 rel begin segment %d\n",i);
fprintf(fff,"\tend.width = 5*seperation\n");
fprintf(fff,"end segment\n");
}
}

```

B.3 MATLAB Code for Computing the Fourier Coefficients of a Trapezoidal Structure

The following MATLAB code is used to calculate the Fourier coefficients. In this specific example, the structure considered is a trapezoid. This code can be modified by replacing the matrix defined in the variable y (in the third block of the code) with 2500 samples of the required shape function $s(z)$ (as defined in APPENDIX. A.1).

```
% Sample code to find the Fourier Coefficient of
% a general trapezoid
clc; clear all; close all;

%% Initialization of variables
max_count=2500; %Grating Period (in nm)
mmax=16; % Number of diffraction orders to be plotted
m=1:mmax;
angle_in_degree=90-10; %90 for perfect vertical
angle=angle_in_degree*pi/180; %angle in radians
etch_depth=300; %Grating etch depth(in nm)

%%Defining the Trapezoidal structure
y1=ceil(etch_depth/tan(angle)); %end of 1st slope of trapezoid
y2=max_count/2-ceil(etch_depth/tan(angle));
%begining of 2nd slope of trapezoid
for i=1:y1    y(i)=tan(angle)*i; end
for i=y1+1:y2    y(i)=etch_depth; end
for i=y2+1:max_count/2    y(i)=etch_depth-tan(angle)*(i-y2); end
for i=max_count/2+1:max_count    y(i)=0; end
y_max=max(y); y=y/y_max; %Normalizing

%% Finding the FFT
```

```

F=2*abs(fft(y))/max_count;
F=F/max(F);

%% Plotting the Fourier Coefficient
j=1; figure(j) ; stem(m-1,F(1:mmax))
grid on;
title('Fourier Coefficient (Trapezoidal)
      as a function of Order','fontsize',14,'fontweight','bold')
xlabel('order - m','fontsize',14,'fontweight','bold')
ylabel('Fourier Coefficient-Trapezoidal',
       'fontsize',14,'fontweight','bold')
saveas(gcf,'FourierCoefficient-Trapezoidal.jpg')
saveas(gcf,'FourierCoefficient-Trapezoidal.fig')

%% Plotting the Shape (for verification)
j=j+1; figure(j) ; stem(y)
title('Shape-Trapezoidal','fontsize',14,'fontweight','bold')
xlabel('n','fontsize',14,'fontweight','bold')
ylabel('y(n)','fontsize',14,'fontweight','bold')
saveas(gcf,'Shape-Trapezoidal.jpg')
saveas(gcf,'Shape-Trapezoidal.fig')

```

APPENDIX C

FABRICATION CHEMISTRY

C.1 Photoresist Developer

The photoresist developer is $\sim 0.1\text{M}$ NaOH solution. The steps for preparing the developer solution for developing ~ 5 samples:

- Take 200 ml DI water.
- Dissolve 4 pellets of NaOH (each pellet weighs ~ 180 mg) in it.
- Stir well and wait for 5 min. until there are no particles left in the solution.

C.2 Chromium Etchant

Chromium etchant is a diluted stock solution of Ammonium Ceric Nitrate and glacial Acetic Acid. The steps for preparing chromium etchant sufficient for developing a $10\text{ cm} \times 10\text{ cm}$ chromium mask is:

- Make the following two mixtures
 - 8 g Ammonium Ceric Nitrate + 30 ml DI water
 - 3 ml glacial Acetic Acid + 35 ml DI water
- Mix them together and dilute the mixture with DI water in the ratio - stock solution:DI water::2:1

C.3 Piranha Solution

Piranha etch is a strong oxidizing agent which removes organic impurities as well as forms a hydrophilic oxide layer on the Si substrate. Its composition is $\text{H}_2\text{SO}_4:\text{H}_2\text{O}_2::3:1$.

REFERENCES

- [1] G. E. Keiser, “A review of WDM technology and applications,” *Optical Fiber Technology*, vol. 5, no. 1, pp. 3–39, 1999.
- [2] B. Mukherjee, “WDM optical communication networks: Progress and challenges,” *IEEE Journal on selected Areas in Communications*, vol. 18, no. 10, pp. 1810–1824, 2000.
- [3] B. Lee, “Review of the present status of optical fiber sensors,” *Optical Fiber Technology*, vol. 9, no. 2, pp. 57–79, 2003.
- [4] G. Gauglitz, “Direct optical sensors: principles and selected applications,” *Analytical and bioanalytical chemistry*, vol. 381, no. 1, pp. 141–155, 2005.
- [5] L. Eldada, “Optical communication components,” *Review of Scientific Instruments*, vol. 75, no. 3, pp. 575–593, 2004.
- [6] R. Alferness, “Guided-wave devices for optical communication,” *IEEE Journal of Quantum Electronics*, vol. 17, no. 6, pp. 946–959, 1981.
- [7] H. Rong, A. Liu, R. Jones, O. Cohen, D. Hak, R. Nicolaescu, A. Fang, and M. Paniccia, “An all-silicon Raman laser,” *Nature*, vol. 433, no. 7023, pp. 292–294, 2005.
- [8] R. Soref, “Reconfigurable integrated optoelectronics,” *Advances in OptoElectronics*, pp. 1–15, 2011.
- [9] L. He, Y. Liu, C. Galland, A. E.-J. Lim, G.-Q. Lo, T. Baehr-Jones, and M. Hochberg, “A high-efficiency nonuniform grating coupler realized with 248-nm optical lithography,” *IEEE Photonics Technology Letters*, vol. 25, no. 14, pp. 1358–1361, 2013.
- [10] V. M. Passaro, F. Magno, and A. Tsarev, “Investigation of thermo-optic effect and multi-reflector tunable filter/multiplexer in SOI waveguides,” *Optics Express*, vol. 13, no. 9, pp. 3429–3437, 2005.
- [11] S. Wang, “Principles of distributed feedback and distributed Bragg-reflector lasers,” *IEEE Journal of Quantum Electronics*, vol. 10, no. 4, pp. 413–427, 1974.
- [12] Z. Wu, S. Honda, J. Matsui, K. Utaka, T. Edura, M. Tokuda, K. Tsutsui, and Y. Wada, “Tunable wavelength-band switch using large coupling-coefficient Bragg grating on SOI rib waveguide,” in *IEEE International Conference on Photonics in Switching*, 2006, pp. 1–3.

- [13] X. Chen, K. Zhou, L. Zhang, and I. Bennion, "Optical chemsensor based on etched tilted Bragg grating structures in multimode fiber," *Photonics Technology Letters*, vol. 17, no. 4, pp. 864–866, 2005.
- [14] K. Rutkowska, D. Duchesne, M. Strain, R. Morandotti, M. Sorel, and J. Azaña, "Ultra-fast all-optical integrated differentiators in Bragg gratings," in *Photonics Global Conference (PGC)*, 2010, pp. 1–4.
- [15] J. Goeckeritz and S. Blair, "Optical characterization of coupled resonator slow-light rib waveguides," *Optics Express*, vol. 18, pp. 18 190–18 199, 2010.
- [16] R. K. Navalakhe, N. DasGupta, and B. K. Das, "Fabrication and characterization of straight and compact Si bend optical waveguides on a silicon-on-insulator platform," *Applied optics*, vol. 48, no. 31, pp. G125–G130, 2009.
- [17] J. P. George, N. Dasgupta, and B. K. Das, "Compact integrated optical directional coupler with large cross section silicon waveguides," in *Proceedings of SPIE Photonics Europe*, 2010, pp. 77 191X–77 191X–8.
- [18] I. S. Krubhakar, R. Narendran, and B. K. Das, "Design and fabrication of integrated optical 1×8 power splitter in SOI substrate using large cross-section single-mode waveguides," pp. 81 730C–81 730C–6.
- [19] G. R. Bhatt and B. K. Das, "Improvement of polarization extinction in silicon waveguide devices," *Optics Communications*, vol. 285, no. 8, pp. 2067–2070, 2012.
- [20] G. R. Bhatt, R. Sharma, U. Karthik, and B. K. Das, "Dispersion-free SOI interleaver for DWDM applications," *Journal of Lightwave Technology*, vol. 30, no. 1, pp. 140–146, 2012.
- [21] P. Sakthivel, N. Dasgupta, and D. BK, "Simulation and experimental studies of diffusion dopped p-i-n structures for silicon photonics," in *SPIE OPTO*, 2013, pp. 8629–16.
- [22] T. E. Murphy, J. T. Hastings, and H. I. Smith, "Fabrication and characterization of narrow-band Bragg-reflection filters in silicon-on-insulator ridge waveguides," *Journal of Lightwave Technology*, vol. 19, no. 12, pp. 1938–1942, 2001.
- [23] P. Heimala, T. Aalto, S. Yliniemi, J. Simonen, M. Kuittinen, J. Turunen, and M. Leppihalme, "Fabrication of Bragg grating structures in silicon," *Physica Scripta*, vol. 2002, no. T101, p. 92, 2002.
- [24] X. Wang, W. Shi, R. Vafaei, N. A. Jaeger, and L. Chrostowski, "Uniform and sampled Bragg gratings in SOI strip waveguides with sidewall corrugations," *Photonics Technology Letters*, vol. 23, no. 5, pp. 290–292, 2011.
- [25] M. Bulk, A. Knights, P. Jessop, P. Waugh, R. Loiacono, G. Mashanovich, G. Reed, and R. Gwilliam, "Optical filters utilizing ion implanted Bragg gratings in SOI waveguides," *Advances in Optical Technologies*, 2008.

- [26] I. Giunttoni, D. Stolarek, H. Richter, S. Marschmeyer, J. Bauer, A. Gajda, J. Bruns, B. Tillack, K. Petermann, and L. Zimmermann, “Deep-uv technology for the fabrication of bragg gratings on soi rib waveguides,” *Photonics Technology Letters, IEEE*, vol. 21, no. 24, pp. 1894–1896, Dec 2009.
- [27] A. Yariv and P. Yeh, *Photonics: Optical Electronics in Modern Communications*. Oxford University Press, 2006.
- [28] G. T. Reed, *Silicon Photonics: An Introduction*. Wiley, 1999.
- [29] D. Taillaert, F. Van Laere, M. Ayre, W. Bogaerts, D. Van Thourhout, P. Bienstman, and R. Baets, “Grating couplers for coupling between optical fibers and nanophotonic waveguides,” *Japanese Journal of Applied Physics*, vol. 45, no. 8A, pp. 6071–6077, 2006.
- [30] V. Ramaswamy, “Strip-loaded film waveguide,” *The Bell System Technical Journal*, vol. 53, pp. 697–705, 1974.
- [31] M. Robertson, S. Ritchie, and P. Dayan, “Semiconductor waveguides: analysis of optical propagation in single rib structures and directional couplers,” in *IEE Proceedings*, vol. 132, no. 6, 1985, pp. 336–342.
- [32] B. Rahman and J. Davies, “Vector-H finite element solution of GaAs/GaAlAs rib waveguides,” in *IEE Proceedings*, vol. 132, no. 6, 1985, pp. 349–353.
- [33] M. Stern, “Semivectorial polarised finite difference method for optical waveguides with arbitrary index profiles,” in *IEE Proceedings*, vol. 135, no. 1. IET, 1988, pp. 56–63.
- [34] P. W. McIlroy, M. S. Stern, and P. C. Kendall, “Spectral index method for polarized modes in semiconductor rib waveguides,” *Journal of Lightwave Technology*, vol. 8, no. 1, pp. 113–117, 1990.
- [35] S. P. Pogossian, L. Vescan, and A. Vonsovici, “The single-mode condition for semiconductor rib waveguides with large cross section,” *Journal of Lightwave Technology*, vol. 16, no. 10, pp. 1851–1853, 1998.
- [36] RSoft-FemSIMTM, <http://optics.synopsys.com/rsoft/rsoft-passive-device-femsim.html>.
- [37] C. Kittel, *Introduction to solid state Physics*. Wiley New York, 1986.
- [38] RSoft-CADTM, <http://optics.synopsys.com/rsoft/rsoft-cad-environment.html>.
- [39] E. J. Walker, “Reduction of photoresist standing-wave effects by post-exposure bake,” *IEEE Transactions on Electron Devices*, vol. 22, no. 7, pp. 464–466, 1975.
- [40] R. Legtenberg, H. Jansen, M. de Boer, and M. Elwenspoek, “Anisotropic reactive ion etching of silicon using SF₆/O₂/CHF₃ gas mixtures,” *Journal of The Electrochemical Society*, vol. 142, no. 6, pp. 2020–2028, 1995.

- [41] I. Richter, P. C. Sun, F. Xu, and Y. Fainman, “Design considerations of form birefringent microstructures,” *Applied Optics*, vol. 34, no. 14, pp. 2421–2429, 1995.
- [42] I. Giuntori, M. Krause, H. Renner, J. Bruns, A. Gajda, E. Brinkmeyer, and K. Petermann, “Numerical survey on Bragg reflectors in silicon-on-insulator waveguides,” in *5th IEEE International Conference on Group IV Photonics*, 2008, pp. 285–287.
- [43] D. J. Griffiths, *Introduction to Electrodynamics*. Prentice Hall, 2006.

LIST OF PUBLICATIONS

S. Harish, D. Venkitesh and B. K. Das, "Highly Efficient DBR in Silicon Waveguides with Eleventh Order Diffraction," *Proceedings of SPIE*, pp. 86290H-86290H, (2013). (Presented in Photonics West 2013, San Francisco, California.)

CURRICULUM VITAE

NAME : Harish Sasikumar

DATE OF BIRTH : 11th July 1988

EDUCATIONAL QUALIFICATIONS

Master of Science (Research)

Institute : Indian Institute of Technology, Madras

Specialization : Electrical Engineering

Year : 2013

Bachelor of Technology

University : University of Calicut

Specialization : Electronics and Communication

Year : 2010

GENERAL TEST COMMITTEE

CHAIR PERSON : Dr. Anil Prabhakar
Professor
Department of Electrical Engineering

GUIDES : Dr. Deepa Venkitesh
Assistant Professor
Dept. of Electrical Engineering

: Dr. Bijoy Krishna Das
Associate Professor
Dept. of Electrical Engineering

MEMBERS : Dr. Harishankar Ramachandran
Professor
Dept. of Electrical Engineering

: Dr. M. P. Kothiyal
Professor
Dept. of Physics